CrossMark

Thermal Fatigue Evaluation of Pb-Free Solder Joints: Results, Lessons Learned, and Future Trends

RICHARD J. COYLE [iD],[1,4] KEITH SWEATMAN,[2] and BABAK ARFAEI[3]

1.—Alcatel-Lucent Bell Labs, Murray Hill, NJ, USA. 2.—Nihon-Superior, Osaka, Japan. 3.—Universal Instruments Corporation, Conklin, NY, USA. 4.—e-mail: richard.coyle@ alcatel-lucent.com

Thermal fatigue is a major source of failure of solder joints in surface mount electronic components and it is critically important in high reliability applications such as telecommunication, military, and aeronautics. The electronic packaging industry has seen an increase in the number of Pb-free solder alloy choices beyond the common near-eutectic Sn-Ag-Cu alloys first established as replacements for eutectic SnPb. This paper discusses the results from Pb-free solder joint reliability programs sponsored by two industry consortia. The characteristic life in accelerated thermal cycling is reported for 12 different Pb-free solder alloys and a SnPb control in 9 different accelerated thermal cycling test profiles in terms of the effects of component type, accelerated thermal cycling profile and dwell time. Microstructural analysis on assembled and failed samples was performed to investigate the effect of initial microstructure and its evolution during accelerated thermal cycling test. A significant finding from the study is that the beneficial effect of Ag on accelerated thermal cycling reliability (measured by characteristic lifetime) diminishes as the severity of the accelerated thermal cycling, defined by greater ΔT, higher peak temperature, and longer dwell time increases. The results also indicate that all the Pb-free solders are more reliable in accelerated thermal cycling than the SnPb alloy they have replaced. Suggestions are made for future work, particularly with respect to the continued evolution of alloy development for emerging application requirements and the value of using advanced analytical methods to provide a better understanding of the effect of microstructure and its evolution on accelerated thermal cycling performance.

INTRODUCTION

In July 2006, the consumer electronic market transitioned to Pb-free solder assembly in order to comply with the European Union Restriction on Hazardous Substances (RoHS) Directive. Provisional exemptions allowed the transition to proceed at a slower pace in high reliability markets such as telecommunication, military, aeronautics, and medical. The transition now has accelerated for high reliability end users as it becomes increasingly difficult to take advantage of the exemption when the supply chain is dominated by the high volume consumer market that is demanding Pb-free components and materials. Uncertainty about whether the exemptions will be renewed after their

scheduled expiration in July 2016 has provided additional motivation for manufacturers of exempt products to convert to Pb-free solders. The successful use of Pb-free solders in an increasingly wide range of applications beyond consumer electronics means that it is difficult to sustain the exemptions on the basis of concern about their reliability compared with the incumbent SnPb solder.

At the time the RoHS directive was enacted, the prevailing opinion was that a high Ag, near-eutectic, Sn-Ag-Cu (SAC) solder alloy was needed to meet the high reliability requirement for low cycle, thermal fatigue resistance. Thermal fatigue is a major source of failure of surface mount (SMT) components and it is critically important in many high reliability applications. Solder joint fatigue failures

(Published online September 8, 2015)

occur due to the coefficient of thermal expansion (CTE) mismatch between the component and the printed circuit board (PCB).[1] Although industry consortia had identified the Sn-Ag-Cu eutectic (nominally Sn3.8Ag0.7Cu) as the best option, the alloy that was used most widely in the first phase of implementation was the slightly hypoeutectic SAC305 alloy (Sn3.0Ag0.5Cu). SAC305 was endorsed by both the Japanese Electronics Industry Association (JEITA) and the IPC Solder Product Value Council (SPVC). The latter is an industry working group comprised primarily of solder suppliers. The decision to use SAC305 was supported by the results of a study sponsored by the IPC SPVC that consisted of limited accelerated thermal cycling and thermal shock testing of three SAC alloys that had Ag content equal to or greater than 3 wt.%.[2] The objective of the study was the minimization of the cost of the alloy by using no more Ag than was necessary to achieve a satisfactory level of performance. While this study satisfied the accelerated thermal cycling requirements of the consumer market, many high-reliability end users did not consider it comprehensive or rigorous enough to justify a transition to SAC solder for their applications.

Soon after the Pb-free transition began, mainstream volume manufacturing and field experiences in consumer markets revealed several shortcomings of near-eutectic SAC, most notably poor mechanical shock performance. In addition to poor shock performance, the cost of SAC305 remained high compared to the SnPb alloy it was replacing, and there were process disadvantages such as rapid dissolution of Cu substrates, shrinkage cracks in fillets resulting from its distinctly non-eutectic solidification behavior and high dross rates in wave soldering. These problems provided an incentive to find alloys better suited to some of the wide range of soldering processes used in electronics assembly.

Consequently, there was a sudden increase in the number of Pb-free solder alloys offered by solder suppliers or reported in the scientific literature. The increasing number of Pb-free alloys provided opportunities to address shortcomings of SAC305 in consumer applications, but this alloy proliferation raised further concerns among high reliability end users that had yet to be convinced of the acceptable long-term reliability of the SAC305.

The high level of susceptibility of electronic assemblies manufactured with SAC305 to failure in drop impact loading was attributed to its higher strength, modulus, and work hardening, which is presumed to be due to the strengthening effect of Ag. The straightforward solution was to reduce the level of Ag in the alloy to around 1% or below while maintaining a nominal Cu content of 0.5%. However, results from early studies[3–6] suggested a decrease in thermal fatigue performance with decreasing Ag concentration. Another trend was the increasing use of microalloying additions to Sn-based alloys. The powerful effect of an addition of Ni at a level previously considered too low to have any significant effect on the behavior of a solder alloy[7] prompted solder manufacturers to experiment with additions of a wide range of other elements including Al, Zn, Mn, Ti, as well as certain rare earth elements.[8,9] Microalloy additions are often paired with lower Ag content, but there is no clear understanding of the impact on thermal fatigue reliability. Furthermore, most of these early investigations lacked benchmarking against eutectic SnPb, raising concern that some low Ag alloys might perform worse than the traditional SnPb in accelerated thermal cycling.

The rapid alloy development drove high reliability end users to address the gaps in the Pb-free thermal fatigue test data. The standard technique for assessing susceptibility to low cycle, thermal fatigue of electronic assemblies is accelerated temperature cycling (ATC), often referred to simply as accelerated thermal cycling. The objective of an ATC test is to accelerate the fatigue damage mechanism to occur in substantially less time than in service. This is a specialized and expensive type of fatigue testing that is performed on daisy-chained components soldered to custom test boards.[10] Due to the number of alloys, costs, resource limitations, overall scope, and time required, the most efficient way of getting this work done was by collaboration through industry consortia. Two of the most comprehensive Pb-free solder reliability programs are being conducted by iNEMI (International Electronics Manufacturing Initiative) and the Universal Instruments A.R.E.A. (Advanced Research in Electronic Assemblies) consortium.

This paper discusses accelerated thermal cycling results from the iNEMI-sponsored Pb-Free Alloy Characterization project. The results are discussed in terms of the goals of the investigation and the relationships among alloy composition, accelerated thermal cycling performance, and microstructural evolution during accelerated thermal cycling. Universal has collaborated with this study to perform advanced microstructural analysis using metallographic techniques not routinely used in the electronics industry at the time the project was being planned. Suggestions are made for future work, particularly with respect to the continued evolution of alloy development for emerging application requirements and the value of using advanced analytical methods to provide a better understanding of the effect of microstructure on accelerated thermal cycling performance.

TEST STRATEGY

Accelerated temperature cycling (ATC) methods were developed for evaluating the thermal fatigue performance of SnPb surface mount solder attachments[10] and a considerable amount of supporting data has been generated for SnPb solder over

decades of testing. Despite significant efforts across the industry, less thermal fatigue data exist for Sn-based, Pb-free solders. Development of comparable data for Pb-free solders has been inhibited at least in part because the industry has been unable to reach consensus on the test methods and parameters. The lack of agreement on Pb-free test parameters is related to the observation that the microstructure, creep, and fatigue behavior of SAC solders are so different from SnPb solder that the test requirements developed for SnPb solder may not be applicable.[10]

The iNEMI Pb-Free Alloy Characterization project was launched in 2008 and is the largest industry-sponsored accelerated thermal cycling program to date. The alloys included in this program are shown in Table I, and the temperature cycling profiles are shown in Table II. The results and details of the experiment have been documented in a series of other publications.[11–19]

The fundamental objective of this project is to provide engineering guidance for the transition to Pb-free solder assembly in the electronics industry. To address that high-level objective, the accelerated thermal cycling investigation includes the following specific, detailed tasks:

- Evaluate the dependence of thermal fatigue reliability on Ag content in the range of 0 to 4%. For Sn-based, Pb-free alloys, the processes of microstructural evolution, creep, and thermal fatigue are known to be dependent on the alloy composition, particularly the Ag content.[3–6]
- Evaluate the effect of accelerated thermal cycling profile, particularly test dwell time, on accelerated thermal cycling performance. Industry accelerated thermal cycling protocols were developed to evaluate the fatigue performance of SnPb eutectic solder and there were concerns about whether those protocols were directly applicable to Pb-free alloys. The creep rate of SAC solders typically is much slower than that of SnPb solder.[20] Therefore, increasing the dwell time might be expected to decrease the life in accelerated thermal cycling of Pb-free solders by providing more time for creep to proceed, thus reducing the number of cycles to failure.[21,22]
- Provide a limited set of data on the relationship between package design and its effect on the solder ball strain and the relative alloy performance. Two different ball grid array (BGA) package constructions with different die to package ratios were used.
- Evaluate the impact of a Ni, Mn, Sb, and Bi microalloying additions on thermal fatigue performance.
- Benchmark the performance of Pb-free alloys against that of eutectic SnPb.

At the onset of the project, the relationship between reliability and microstructure was not a major focus. The primary objective was to provide practical reliability data on candidate alloys rather than explore the metallurgy of the various solder formulations selected. The role of microstructure and microstructural evolution during accelerated thermal cycling received greater attention as the project progressed and microstructural data emerged from other research sources. During accelerated thermal cycling the microstructures of SAC alloys evolve continually by coarsening of Ag_3Sn and Cu_6Sn_5 particles and recrystallization of Sn grains in areas of stress concentration where most of the strain occurs.[23–26] The combined effect of this microstructural evolution appears to be a reduction in resistance to creep and thermal fatigue. In the cases where the initial solder microstructure is more resistant to microstructural evolution during thermal exposure, the solder joint resistance to thermal fatigue is much less likely to change over time.[22]

Table I. The alloys tested and their nominal compositions

BGA ball alloy composition	Trade name
Sn-37Pb	SnPb
Sn-0.7Cu-0.05Ni + Ge	Sn100C
Sn-0.3Ag-0.7Cu	SAC0307
Sn-0.3Ag-0.7Cu + 0.09Bi	SACX
Sn-1.0Ag-0.5Cu	SAC105
Sn-1.0Ag-0.5Cu + 0.03Mn	SAC105 + Mn
Sn-1.0Ag-0.5Cu + 0.05Ni	SAC105 + Ni
Sn-1.0Ag-0.7Cu	SAC107
Sn-1.7Ag-0.7Cu + 0.4Sb	SACi
Sn-2.0Ag-0.5Cu	SAC205
Sn-2.0Ag-0.5Cu + 0.05Ni	SAC205 + Ni
Sn-3.0Ag-0.5Cu	SAC305
Sn-4.0Ag-0.5Cu	SAC405

Table II. Temperature cycling profiles used in the experimental program

BGA ball alloy composition	Trade name
Sn-37Pb	SnPb
Sn-0.7Cu-0.05Ni + Ge	Sn100C
Sn-0.3Ag-0.7Cu	SAC0307
Sn-0.3Ag-0.7Cu + 0.09Bi	SACX
Sn-1.0Ag-0.5Cu	SAC105
Sn-1.0Ag-0.5Cu + 0.03Mn	SAC105 + Mn
Sn-1.0Ag-0.5Cu + 0.05Ni	SAC105 + Ni
Sn-1.0Ag-0.7Cu	SAC107
Sn-1.7Ag-0.7Cu + 0.4Sb	SACi
Sn-2.0Ag-0.5Cu	SAC205
Sn-2.0Ag-0.5Cu + 0.05Ni	SAC205 + Ni
Sn-3.0Ag-0.5Cu	SAC305
Sn-4.0Ag-0.5Cu	SAC405

Table III. A comparison of the solder ball alloy Ag content analyzed by inductively coupled plasma atomic emission spectroscopy (ICP-AES) and the calculated Ag content after board level assembly with SAC305 solder paste

Solder alloy	Solder ball Ag content			
	84CTBGA[a] analyzed wt.%	84CTBGA[b] effective wt.%	192CABGA[a] analyzed wt.%	192CABGA[b] effective wt.%
Sn-37Pb	0	0	0	0
SN100C	0	0.79	0	0.29
SAC0307	0.31	1.00	0.31	0.57
SAC0307 + Bi	0.31	1.00	0.28	0.54
SAC105	0.99	1.50	1.01	1.20
SAC105 + Ni	0.93	1.46	0.93	1.13
SAC105 + Mn	0.94	1.48	0.95	1.14
SAC107	1.01	1.50	1.00	1.19
SAC205	1.92	2.19	1.99	2.09
SAC205 + Ni	1.97	2.23	1.99	2.07
SACi	1.69	2.04	1.69	1.81
SAC305	2.92	2.94	2.93	2.95
SAC405	3.67	3.69	3.76	3.50

[a]Analyzed (ICP) solder ball Ag content prior to ball attachment on BGA. [b]Calculated solder ball Ag content after board level assembly with SAC305 paste.

Table IV. Physical and design characteristics of the PCB and BGA test vehicles

BGA package (component)

	CABGA192	CTBGA84
Die size (mm)	12 × 12	5 × 5
Body size (mm)	14 × 14	7 × 7
Ball array	16 × 16	12 × 12
Pitch size (mm)	0.8	0.5
Ball diameter (mm)	0.46	0.3
Pad finish	Electrolytic Ni/Au	

Printed circuit board (PCB)

Thickness (mm)		2.36
Surface finish		High temp. OSP
Pad diameter (mm)	0.356	0.254
Solder mask diameter (mm)	0.483	0.381

EXPERIMENTAL PROCEDURES

The BGA component test vehicles were procured as land grid arrays (LGA) to enable subsequent attachments of the various different solder alloy balls.[12] Surface mount assembly for all Pb-free alloys was done using SAC305 paste. At the time, matching solder paste formulations were not available for all the alloys and SAC305 was the prevailing assembly choice throughout the industry. In all cases except SAC305, this resulted in a solder joint composition different from the original solder ball with the difference being greater with the smaller

solder ball of the CTBGA84 (Table III). Thus, assembly with the SAC305 solder paste precluded an absolute comparison of alloy compositions.

The components and the test circuit boards were daisy-chained to allow in situ, continuous resistance monitoring during accelerated thermal cycling. A sample size of 16 was used for each component type and alloy type. The attributes of the BGA components and printed circuit board that comprise the daisy-chained test vehicle are shown in Table IV.

Accelerated thermal cycling was done in accordance with the IPC-9701A industry test guideline.[10] For all the profiles listed in Table II, assembled circuit boards were thermally cycled from with a ramp rate of 10°C/min between temperature extremes in accordance with the IPC-9701A guidance. The hot and cold dwell times were either 10 min or 60 min. The solder joints were monitored using either an event detector or a data logger and failure was defined by a resistance limit of 1000 ohms. Although great care was taken to precisely define the thermal cycle profile, allowance has to be made for the possibility that results might be affected by the fact that testing was carried out in seven different laboratories.[11]

The CTE of the PCB was measured using a thermo-mechanical analyzer and found to be 13 ppm/°C. The composite CTE of the BGA packages was measured using microscopic Moiré interferometry. The data in Fig. 1 indicates a lower composite CTE for the 192CABGA package. The lower CTE and the larger distance from neutral point (DNP) of the 192CABGA package result in
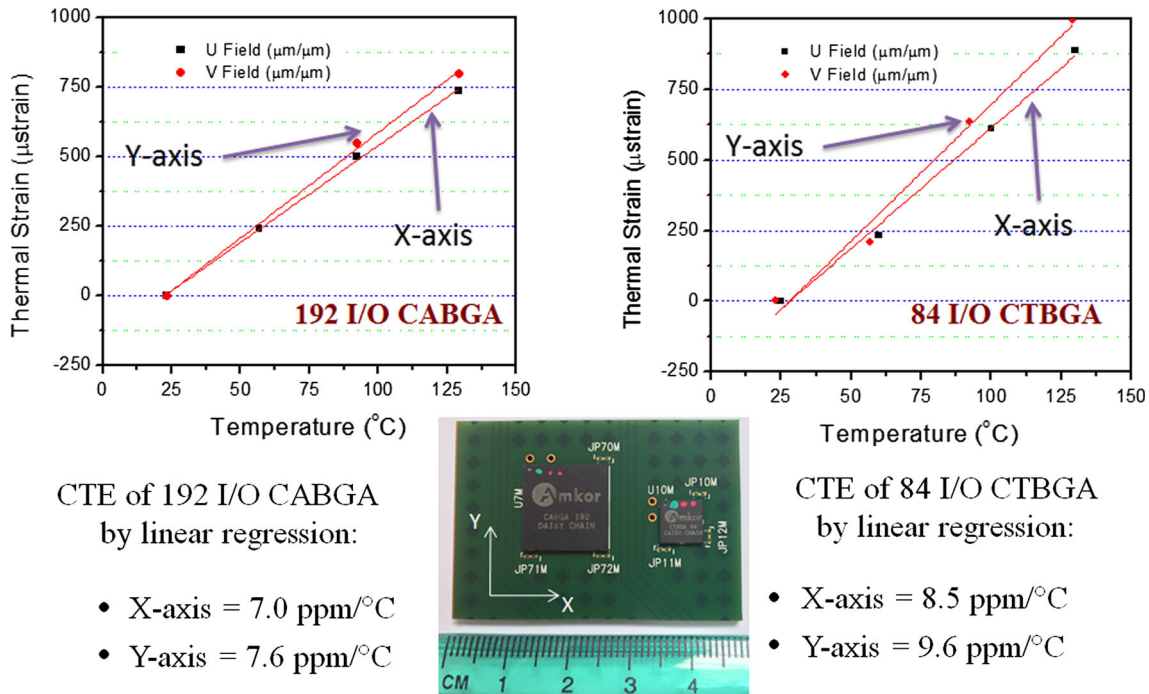
Strains and linear regression curves

Fig. 1. Microscopic Moiré interferometry data illustrating the lower composite CTE of the 192CABGA that results in a greater CTE mismatch between the PCB and component substrate. Measurement of component strain as a function of temperature by the microscopic Moiré technique show that the composite CTE of the 192CABGA is on average about 20% less than that of the 84CTBGA, which means that, due to the greater CTE mismatch with the substrate, joints on the former will be subjected to great strain during thermal cycling.

joints in the outer array being subjected to greater shear strain so that lifetime in thermal cycling is expected to be shorter than that of the 84CTBGA.

A baseline microstructural characterization was performed on representative board level assemblies from each of the component and alloy test cells. The baseline characterization provided a qualitative assessment of the Ag_3Sn particle size and density at time zero (before temperature cycling) for comparison to the microstructure in samples that failed during temperature cycling. Microstructural characterization and failure analysis was done using optical metallography (destructive cross-sectional analysis), polarized light microscopy (PLM), and scanning electron microscopy (SEM). The SEM operating in the backscattered electron imaging mode was used to differentiate phases in the SAC microstructures. Backscattered electron imaging has been shown to be useful in previous studies for differentiating phases in the SAC microstructures.[12,14] Low magnification optical microscopy was adequate for characterizing the eutectic SnPb microstructure and for confirming the thermal fatigue failure mode in all alloys.

ACCELERATED THERMAL CYCLING RESULTS

All the failure data is this paper are reported as characteristic lifetime N63.2, the number of cycles to achieve 63.2% failure from a two-parameter

Weibull analysis. The N63.2 criterion is accepted practice for evaluating this type of wear out data.[10] Typical Weibulls for the two component types are plotted in Fig. 2. If the effect of the early failures of the SAC405 due to assembly defects are ignored the results show a clear trend with the cycles to 63.2% failure (characteristic life) showing a trend clearly related to the Ag content of the alloy. The high β and the generally tight distribution of the data provide a high level of confidence in the results and indicate that the relationship between alloy and cycles to failure extends down to 1% and 5% failure rates.

Effect of Ag Content

Figure 3 illustrates the influence of Ag content on thermal fatigue reliability measured using the common industrial thermal cycle of 0/100°C and −40/125°C. In the 0/100°C cycling the characteristic lifetimes for both packages with the SAC405 alloy (4 wt.% Ag) are approximately twice that for the SN100C (nominally zero Ag but with 0.3–0.8% Ag from the SAC305 assembly paste). The differences in characteristic lifetime between SAC405 and SAC105 are 20% for the 192CABGA and 40% for the 84CTBGA. Less dependence on Ag content in the 192CABGA might be presumed due to higher strain level in this package.

This effect of package type on the performance for a wider range of the tested alloys in the 0/100°C thermal cycle is more apparent in Fig. 4, which also
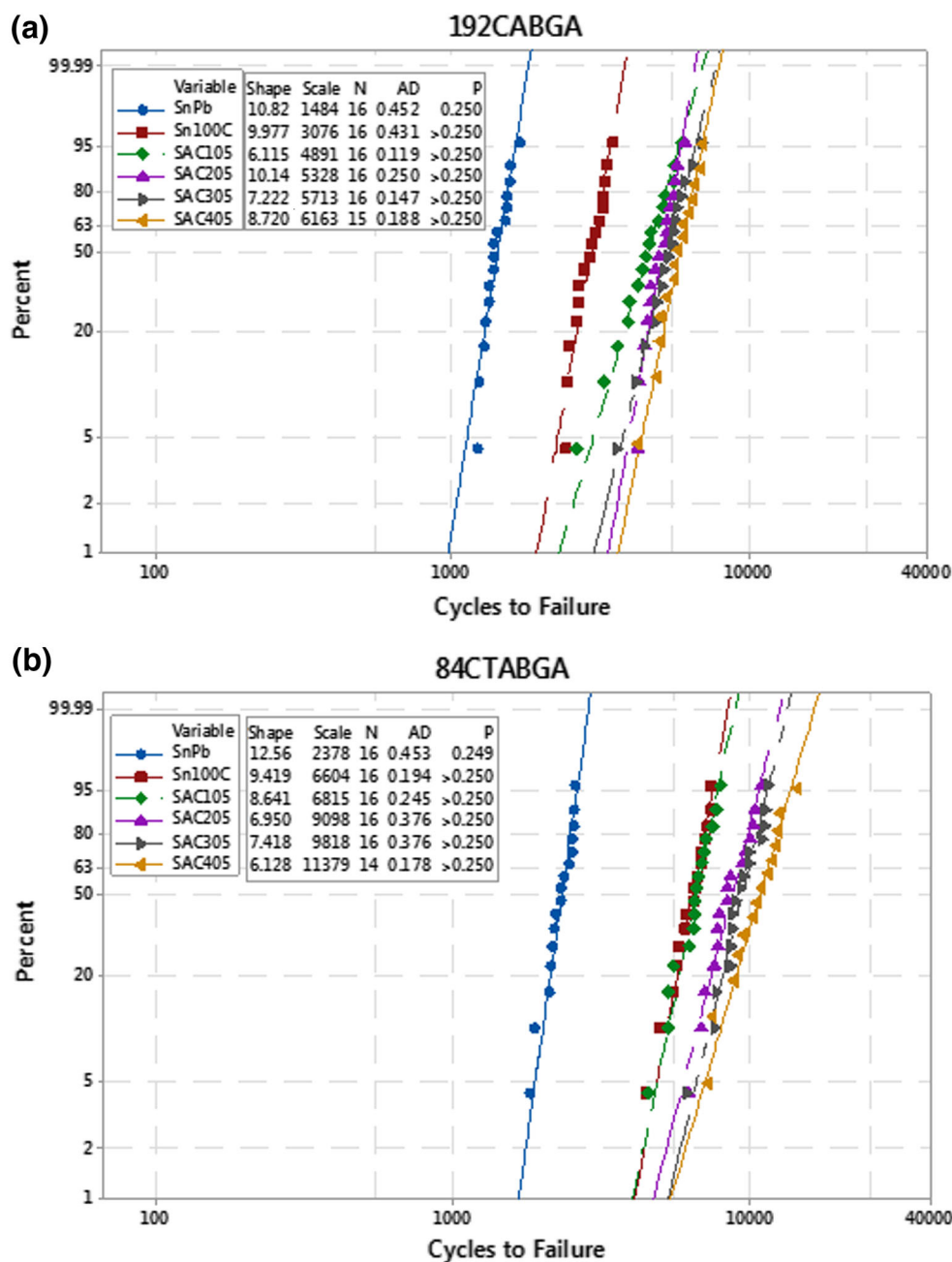
(a)

(b)

Fig. 2. Two-parameter Weibull plots for the 0/100°C thermal cycle with 10-min dwells showing the effect of component type: (a) the 192CABGA and (b) the 84CTBGA. The tabulated characteristic lifetime (scale) is based on the N63.2 failure criterion.

shows the performance with ascending Ag content. In the 192CABGA package, the characteristic life of the alloys is much less sensitive to Ag content than in the 84CTBGA package. These trends are consistent through the entire range of alloys in the experiment (e.g., Fig. 4 for the 0/100°C cycle) as well as with other data from the literature.[3,6,27–30]

There is a clear relationship between characteristic lifetime and Ag content measured in accelerated thermal cycling. This effect is presumed to be due to the dislocation pinning effect of the Ag_3Sn

particles.[9] The effectiveness of the Ag_3Sn particles would be expected to diminish as they coarsen and the interparticle spacing increases as a result of Ostwald ripening. This effect is apparent in the reduction in the advantage in the more aggressive −40/125°C cycle, where the dependence of characteristic lifetime on Ag content is not as dramatic as it is with the 0/100°C cycle with either BGA package. While for the −40/125°C cycle the SAC405 still is about 50% more reliable than the SN100C, the reduction in reliability with decreasing levels of Ag
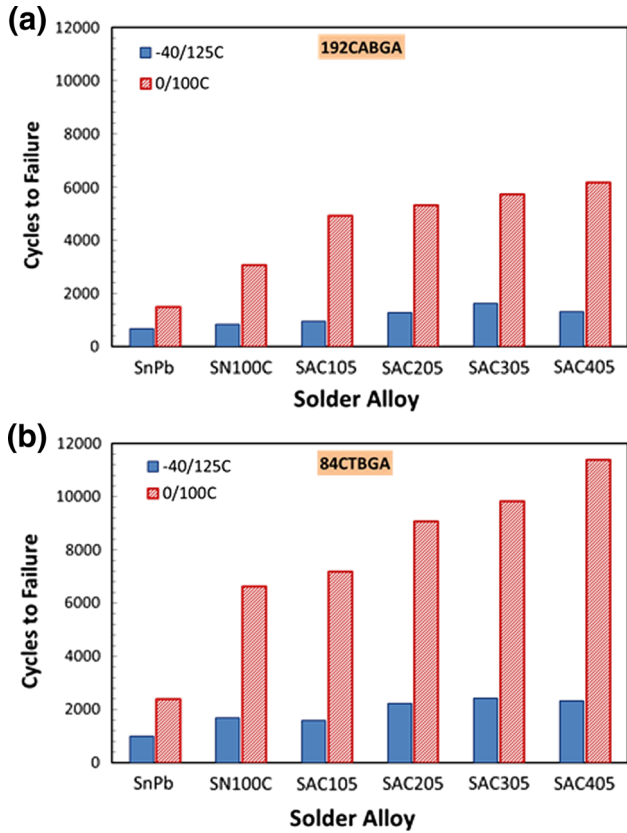
Fig. 3. Comparison of characteristic lifetime (N63.2) as a function of Ag content and thermal cycle profile for (a) the 192CABGA and (b) the 84CTBGA. It is apparent that the strengthening effect of Ag diminishes as the severity of the thermal cycle and the CTE difference between component and substrate increases.
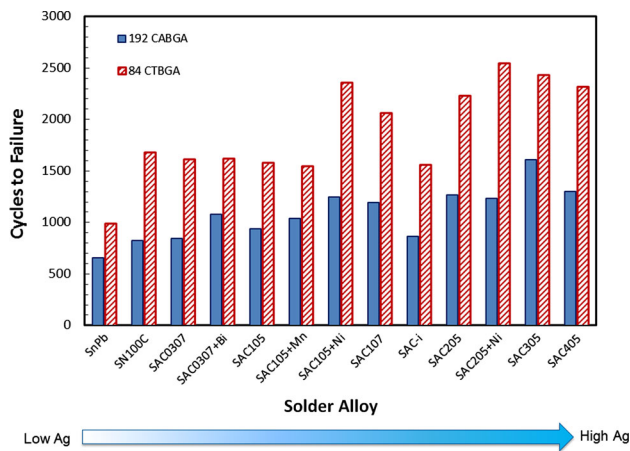

Fig. 4. Characteristic lifetime (N63.2) of all the alloys in the test program with the 0/100°C thermal cycle and 10-min dwell. Results are plotted in order of increasing Ag content with the basic dopant-free variant plotted first.

content is less obvious. In fact, it could be argued that there is minimal statistical difference in reliability between the various Sn based Pb-free alloys in the −40/125°C test. This result is not surprising considering the results reported by Lee and Ma, in

which they observed a minimal difference in performance between SAC305 and SAC105 using a high-strain test vehicle configuration.[31] They concluded that Ag_3Sn precipitate coarsening occurred so rapidly under their test conditions that the Ag content and particle density were no longer the primary factors controlling thermal fatigue life. The results for the −40/125 °C cycle are consistent with the Lee and Ma hypothesis because this severe temperature cycle is characterized by a combination of the highest strain (ΔT) and the highest peak temperature, two factors that are expected to accelerate coarsening of the Ag_3Sn particles.[23–26]

Effect of Component Type

The test data presented in Fig. 5 (as well as Figs. 3 and 4 previously) show clearly that the 84CTBGA outperforms the 192CABGA by a wide margin.[1,22,23] The 192CABGA package construction and very high die to package ratio generate higher shear strains in the solder joints resulting in earlier failures. This is demonstrated by the microscopic Moiré interferometry data in Fig. 1 which shows a lower composite CTE for the 192CABGA. The lower CTE for the 192CABGA results in a larger CTE mismatch with the PCB (nominally 13 ppm/°C measured with a thermo-mechanical analyzer) than in the case of the 84CTBGA. The larger CTE mismatch and greater distance from neutral point drives failure sooner in the case of the 192CABGA. Although the smaller ball of the 84CTBGA package will experience higher effective shear for a given component and substrate strain differential, the shorter distance from the neutral point means that strain differential for solder balls in the outer rows will be smaller. It is not possible to determine the exact influence of each of these factors on the characteristic lifetimes of these alloys but the overall trend is clear. In summary, the effects are qualitatively the same for both packages but quantitatively different because of different package construction, die size, and post-reflow Ag content.

Another factor affecting the difference in performance between the 84CTBGA and the 192CABGA is the effect of the ball size on the final composition of the solder joint reflowed with SAC305 solder pastes. As shown in Table III, the increase in Ag content due to the SAC305 paste is always slightly greater in the 84CTBGA solder spheres compared to the 192CABGA. This complicates the data interpretation and precludes an absolute comparison of alloy compositions.

Effect of ATC Dwell Time

Figures 6 and 7 compare the results for the standard 10-min upper and lower temperature dwell times to the extended 60-min dwell times. These charts show that an increase in accelerated thermal cycling dwell time from 10 min to 60 min
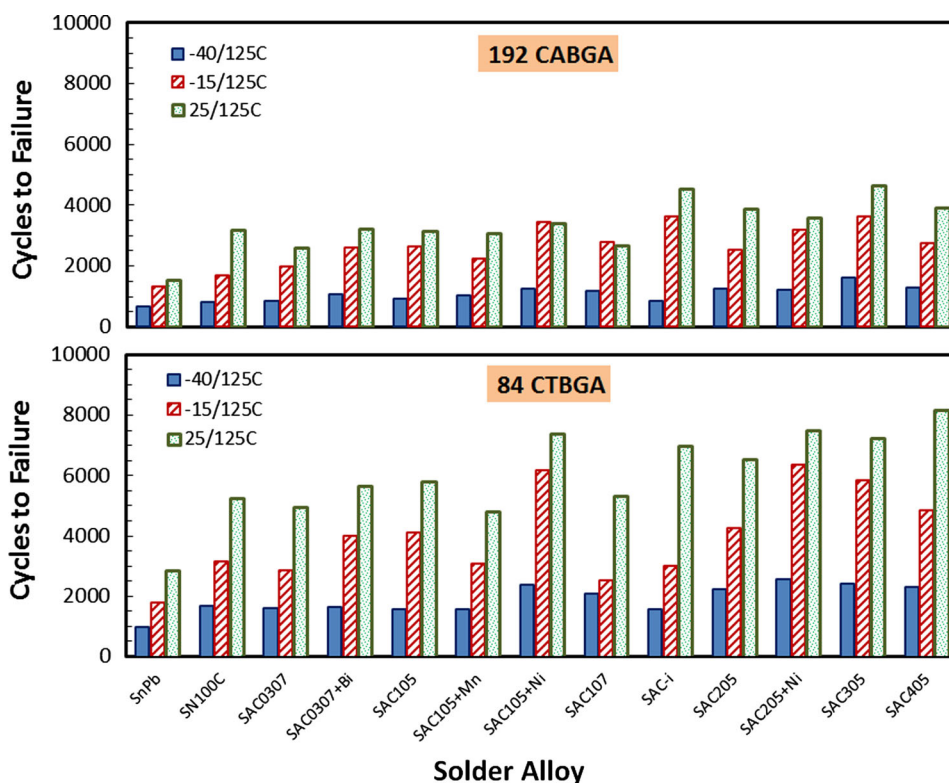
Fig. 5. Characteristic lifetime (N63.2) of all alloys and three thermal cycle profiles with 10-min dwells. Characteristic lifetimes decrease with the severity of the thermal profile in terms of ΔT and peak temperature. In the case of the 192CABGA package, the effect of the increasing severity of the thermal cycle is amplified by the higher strain to which joints are subjected as a result of the larger difference between its CTE and that of the PCB on which it is mounted.

decreases the accelerated thermal cycling reliability of Sn based Pb-free solders. In almost all cases, the reduction in reliability was significant, ranging typically from 25% to 40%. The longer dwell time allows for more creep to occur in each cycle and consequently more of the damage that drives recrystallization. The longer dwell at peak temperature allows more time for the processes of recrystallization and Ag$_3$Sn coarsening and more time for the grain boundary sliding and grain rotation that initiate and propagate cracks. The reduction in characteristic lifetime is expected since these are all processes that lead to failure.

From an application standpoint, a critical objective of the study was to benchmark the performance of Pb-free alloys relative to eutectic SnPb solder. This comparison was especially important with the 60-min dwell time that allows a longer time for creep of the solder. The results in Figs. 6 and 7 show that all the Pb-free solders outperform the SnPb solder even with the extended dwell time.

Effect of ATC Profile

All alloys have by far the longest characteristic lifetime with the mild 0/100°C thermal cycle with the 10-min dwell. Characteristic life drops dramatically with either an increase in the ΔT, or the longer dwell time. The effect of increasing the dwell

time in the −40/100°C thermal cycle is generally much smaller than the effect of increasing dwell time in the 0/100°C thermal cycle. Since the peak temperature at which most of the Ag$_3$Sn coarsening and recrystallization will be occurring is the same, the differences in characteristic lifetime can be attributable only to the greater strain of the cycle with the larger ΔT and the longer time during which recovery processes can occur. Because the trends in Fig. 8 are not consistent quantitatively from alloy to alloy, it is not possible to conclude if ΔT (strain) or dwell time is dominant.

While there are many different predictive models for accelerated thermal cycling performance of Pb-free solders, it is agreed that the shear strain generated in the solder is proportional to the ΔT and the CTE mismatch (e.g., Ref. 32). Predictive models also contain solder constants based on creep activation. Presumably, the larger ΔT generates more strain damage to drive Ag$_3$Sn coarsening and recrystallization, while the longer dwell provides more time for Ag$_3$Sn coarsening and recrystallization to occur.

The sensitivity of the strengthening effect and reliability of Ag content to strain and temperature again is apparent in Fig. 8. For all the alloys containing Ag, the maximum life in accelerated thermal cycling occurs with 0/100°C thermal cycle. This cycling profile has the smallest ΔT and the lowest
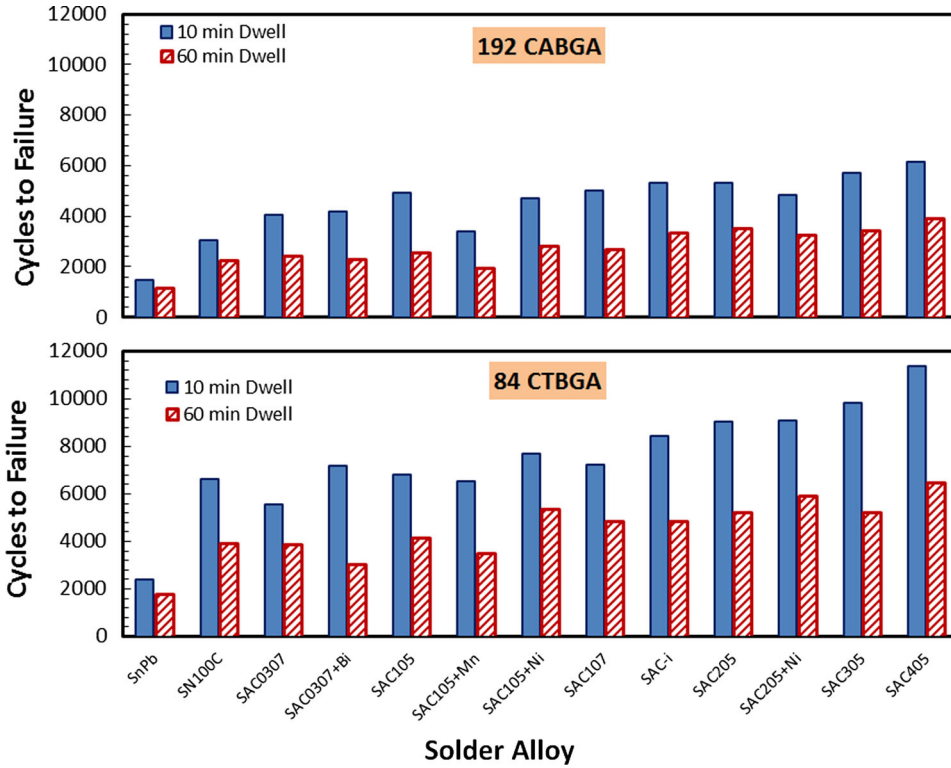
Fig. 6. Characteristic lifetime (N63.2) as a function of dwell time for all alloys tested in thermal cycling with the 0/100°C profile. The reduction in reliability ranges from 25% to 40% across all alloys and component types.
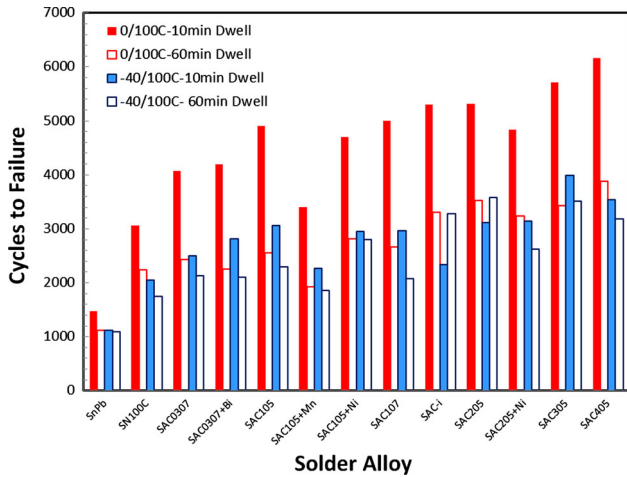

Fig. 7. Effect of thermal cycle and dwell time on characteristic lifetime of all alloys tested with the 192CABGA package. An increase in thermal cycling dwell time from 10 min to 60 min decreases the thermal cycling reliability of all solders with both thermal cycle profiles.
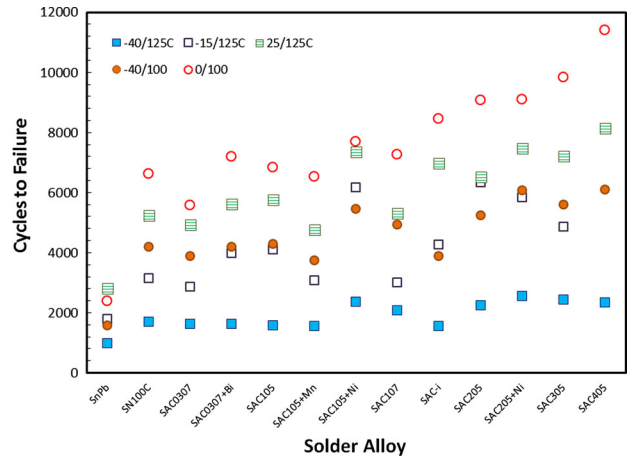

Fig. 8. A comparison of characteristic lifetimes of all alloys tested with five different thermal cycling profiles. The dwell time is 10 min and the component is the 84CTBGA. Both characteristic lifetimes and the strengthening effect of Ag diminish as the severity of the thermal profile increases in terms of ΔT and peak temperature.

peak temperature (0/100°C). With the most severe thermal cycle (−40/125°C) the sensitivity of characteristic lifetime to the Ag content has all but disappeared.

The maximum characteristic lifetimes occur with the least aggressive 0/100°C cycle. Although the trends are not always consistent across all alloys, there is a 20–50% reduction in characteristic

lifetimes with the more aggressive cycles. The magnitude of the reduction in characteristic life from the peak with the 0/100°C thermal cycle increases in the following order:

- For a ΔT of 100°C the peak temperature is increased from 100°C to 125°C
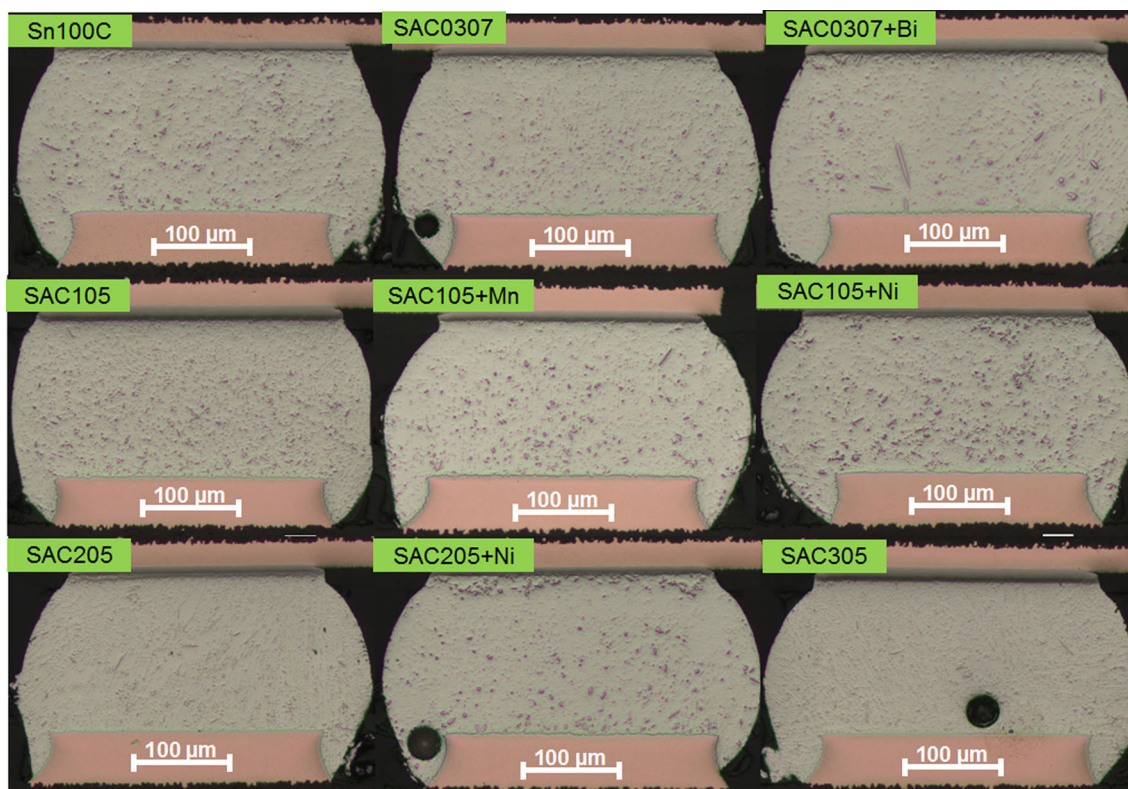- The peak temperature is 100°C but the DT is increased from 100°C to 140°C

Fig. 9. Low-magnification optical micrographs following board level assembly of the 84CTBGA component with the various Pb-free alloys. The dark particles in the light Sn matrix are the Cu_6Sn_5 and Ag_3Sn intermetallic particles but there is no obvious correlation between the Ag content and the apparent volume fraction of particles visible.

- For a ΔT of 140°C the peak temperature is increased from 100°C to 125°C
- The peak temperature is 125C but the ΔT is increase from 140°C to 165°C

The dilemma in interpreting these trends is that there are no data that would make it possible to determine whether strain due to ΔT or dwell time is dominant. Interpretation is complicated further because Ag_3Sn particle coarsening is accelerated substantially faster at the 125°C peak temperature than at 100°C.[33]

MICROSTRUCTURAL ANALYSIS

Assembled Samples

Low magnification optical micrographs of the 84CTBGA component with the various Pb-free alloys after board level assembly are shown in Fig. 9. The intermetallic particles and Sn dendrites can be difficult to resolve with optical microscopy, even at higher magnification as shown Fig. 10 for SAC305. Figure 11 shows high magnification backscattered images of the assembled or baseline BGA solder joint microstructures for the 84 CTBGA package. All micrographs are from areas near the soldered interface at the package side of the component where thermal fatigue cracking is expected

to initiate and propagate to failure. The large amount of undercooling typically required to nucleate the β-Sn phase tends to suppress the equilibrium ternary eutectic structure in SAC Pb-free alloys.[34] This is true even with SAC305 despite its near-eutectic composition.[35]

The microstructures in Fig. 11 consist of Ag_3Sn particles (white phase) on the primary Sn (gray phase) boundaries with the Cu_6Sn_5 intermetallic particles (dark phase) distributed between the interdendritic spaces and generally not located on the primary Sn boundaries. As expected, the number of the Ag_3Sn particles decreases with decreasing Ag content. The Cu_6Sn_5 intermetallic distribution is not regarded as critical because Ag_3Sn particles are the primary microstructural feature that influences thermal fatigue resistance in SAC alloys.[3,6,27,28,36–38]

Solidification of the alloys studied in this project should be considered in relation to the liquidus surface of the tin-rich corner of Sn-Ag-Cu equilibrium phase diagram shown in Fig. 12.[39] The starting points of the five basic alloys, SAC0307, SAC105, SAC205, SAC305 and SAC405 are marked. During solidification under equilibrium conditions, the composition of the remaining liquid moves down the temperature gradient as indicated by the arrows. For the SAC0307, SAC105 and SAC205, the first stage of solidification is the freezing of primary
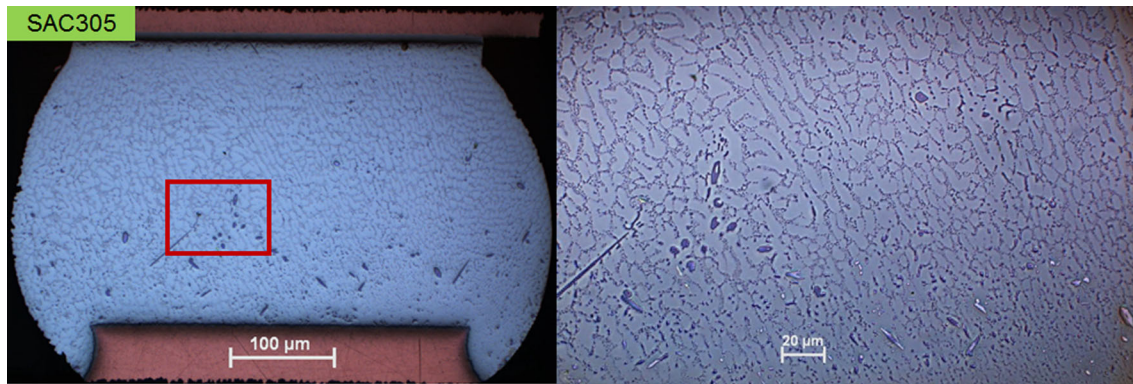
Fig. 10. Bright field optical micrograph of a SAC 305, 192CABGA component after board-level, solder reflow assembly. The higher magnification image (right) was taken from the center of the BGA solder ball shown at the left. This image shows the Sn dendrite structure outlined by fine Ag_3Sn in the interdendritic regions. Larger, randomly located Cu_6Sn_5 precipitates can also be observed.
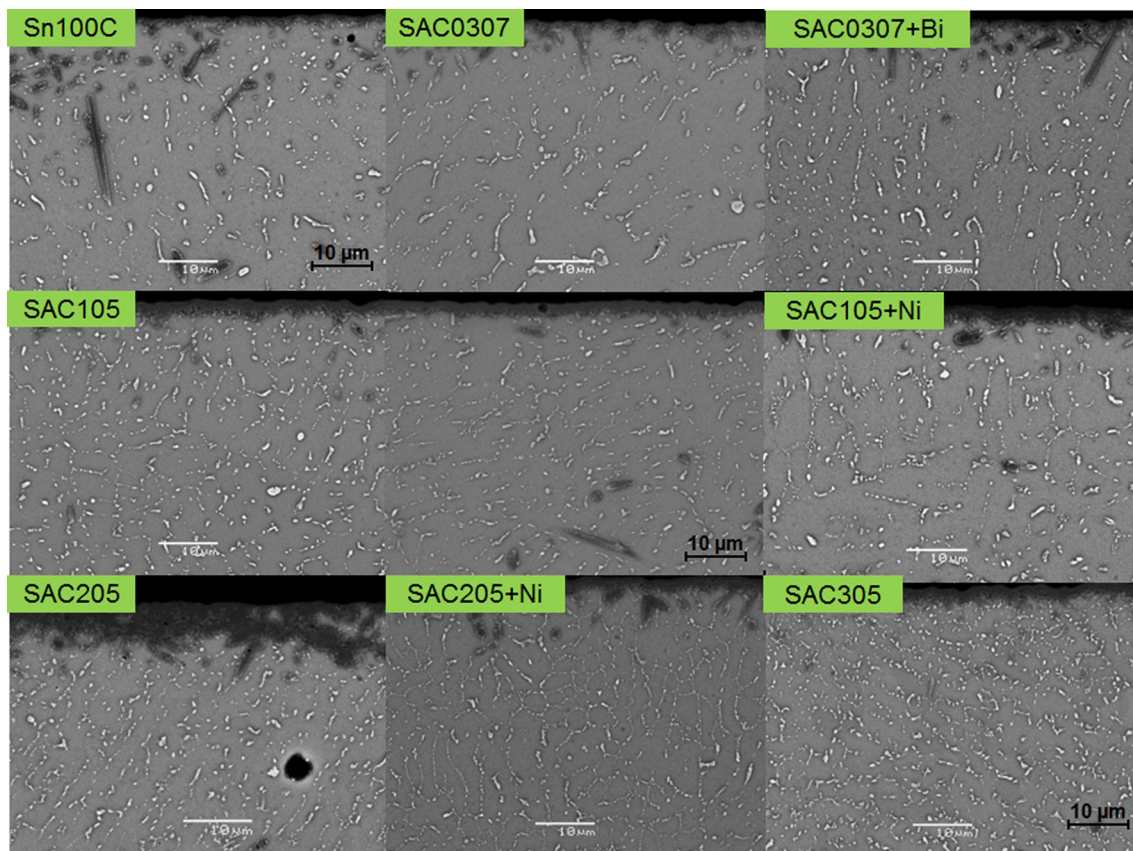

Fig. 11. High-magnification backscattered images of the time zero or baseline 84CTBGA solder joint microstructures for nine different Pb-free alloys.

Sn dendrites until the composition of the remaining liquid reaches the pseudobinary eutectic $Sn-Cu_6Sn_5$. As the solidification of this eutectic proceeds, the composition moves toward the ternary eutectic $Sn-Ag_3Sn-Cu_6Sn_5$ where the remaining liquid solidifies. For SAC305, there is freezing out of primary Sn dendrites until the composition of the remaining liquid reaches the pseudobinary $Sn-Ag_3Sn$ eutectic and the composition of the remaining liquid moves towards the ternary eutectic. For SAC405, the first phase to freeze out is primary Ag_3Sn and the composition of the remaining liquid moves towards the pseudobinary eutectic $Sn-Ag_3Sn$ and solidification with the composition of the remaining liquid moving to the ternary eutectic.

The equilibrium microstructures of the SAC0307, SAC105 and SAC205 should therefore be similar except with regard to the proportion of
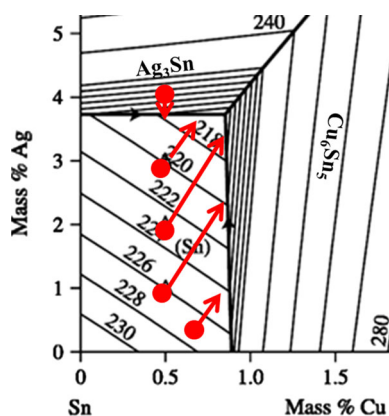
Fig. 12. The liquidus projection of the tin-rich corner of Sn-Ag-Cu equilibrium phase diagram with equilibrium freezing trajectories indicated for SAC0307, SAC105, SAC205, SAC305 and SAC405. The source of this figure is Ref.[39].
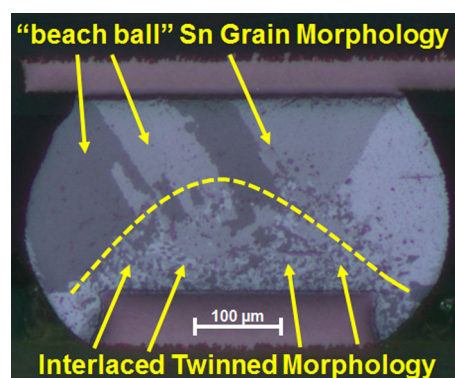

Fig. 13. Photomicrograph obtained using polarized light microscopy (optical images with cross-polarizers) of a SAC405 ball containing regions with beach-ball and interlaced twinned microstructures.

pseudobinary Sn-Cu_6Sn_5 eutectic and ternary Sn-Ag_3Sn-Cu_6Sn_5 eutectic. The microstructure would be dominated by primary Sn dendrites with eutectic phases in the interdendritic regions with small particles of the two intermetallic phases in a Sn matrix. The microstructure of the SAC305 would be similar with the two intermetallic phases formed by eutectic solidification in the interdendritic region. SAC405 would be expected to be largely dendritic with embedded primary Ag_3Sn. The SN100C alloy would be nearly 100% Sn-Cu_6Sn_5 eutectic. The Ni microalloying additions move the otherwise hypoeutectic Sn-0.7C base of the SN100C alloy to eutectic solidification.[7] The effect on reliability in accelerated thermal cycling of the Ni in the SN100C and the SAC105 and SAC205 alloys to which Ni has also been added is not known, but all the Ni would be incorporated in the Cu_6Sn_5 phase, partially substituting for Cu.[40] The effect of the Mn addition to the SAC105 alloy is not clearly known. Bi would be in solid solution in the Sn phase but the effect on solidification behavior at the low level at which it is present is not known.

In practical soldering, equilibrium conditions do not prevail. Although the final volume fractions of the phases are as predicted by the equilibrium phase diagram, the sequence in which they solidify and the solidification mode are different. Because of the difficulty of nucleating Sn the solder usually cools well below the equilibrium liquidus temperature before nucleation occurs. Because there are few nuclei, the solder joints often contain often only a few Sn grains.

The microstructure of SAC305 (Fig. 10) is representative of the microstructure of all of the SAC alloys in that it is made up of a network of primary Sn dendrites. In a cross-section, the shape of the dendrite arms is defined by fine particles of Ag_3Sn in the interdendritic regions (Fig. 10). Under the non-equilibrium conditions, the Cu_6Sn_5 phase appears to be randomly dispersed and of larger

particle size than would be expected from the coupled growth of eutectic solidification. The microstructures of the other alloys are assumed to differ only in the volume fraction of Ag_3Sn in the interdendritic regions (Fig. 11). The volume fraction of Ag_3Sn is proportional to the Ag content of the alloy but its distribution will depend on the solidification sequence that occurs in the non-equilibrium conditions that obtained during reflow soldering.

The Sn grain morphology is another microstructural feature that might affect reliability.[41,42] Figure 13 shows an example of a cross-sectional image of a SAC solder ball obtained with polarized light microscopy (PLM) or cross-polarized imaging. This technique is useful for identifying Sn grain morphology after reflow and solidification. Large scale BGA solder joints generally display one to three large Sn grains, each with a number of dendrites with the same crystallographic orientation.[43,44] Frequently, this is called the "beach ball" morphology. A fine-grain interlaced twinned morphology may also form depending on the solidification conditions.[44] The micrograph with crossed polarizers shown in Fig. 13 contains regions with the large grain, beach ball morphology and the interlaced twinned morphology.

Figure 14 shows optical micrographs with crossed polarizers taken from metallographic samples of the 192CABGA component and nine different Pb-free solder alloys. There is considerable variation in the Sn microstructures for any of the alloy or component combinations, but most of the cross-sections are characterized by either single Sn grains or the "beach ball" Sn grain morphology. Some solder joints contain small regions with the interlaced twinned grain morphology and a few have larger interlaced regions, but the latter is a distinct minority. Interlaced twinning tends to occur more often with the higher Ag content alloys and more in the smaller solder balls of the 84CTBGA component. These observations are consistent with previous studies that have shown a correlation between solidification temperature, alloy composition, and
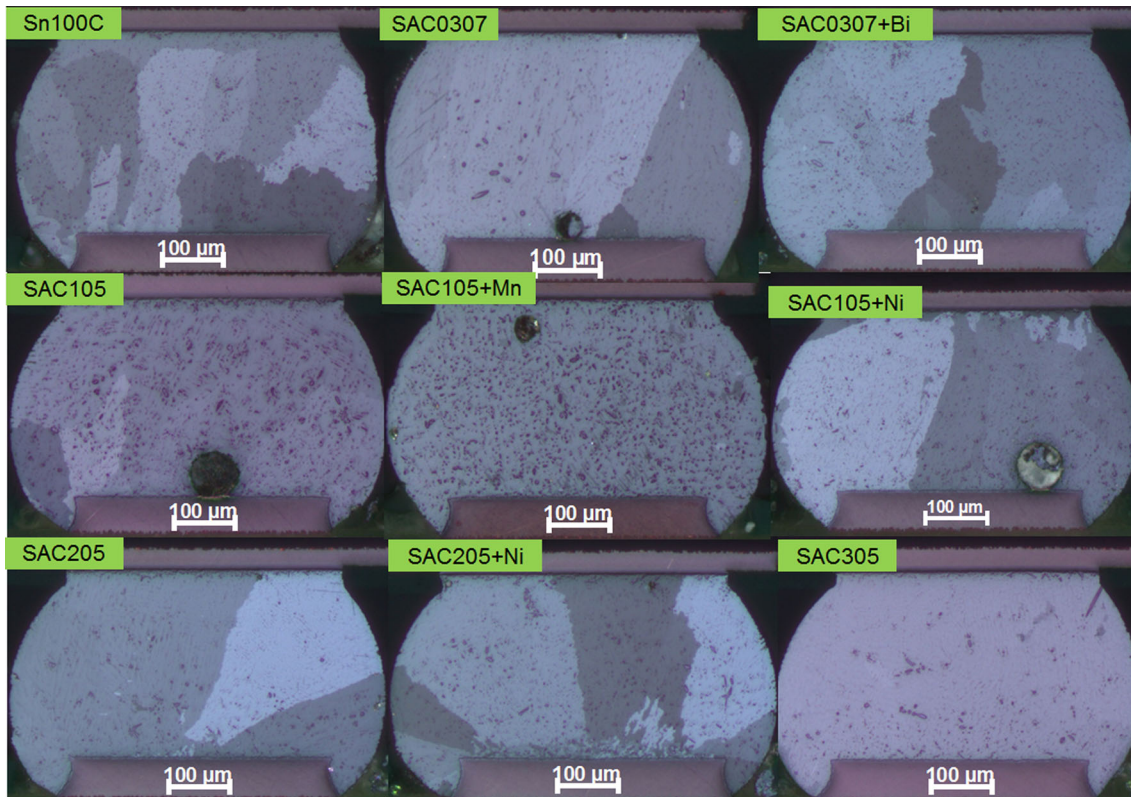
Fig. 14. Optical polarized light images from metallographic samples of the 192CABGA component and nine different Pb-free solder alloys. The Sn grain morphology is mostly single or multiple grain beach-ball type.

the Sn grain morphology in near eutectic SAC alloys.[44] It has been suggested that the fine-grain, interlaced twinned morphology has better thermal fatigue performance,[41,42] but interlaced twinning is sporadic in these samples and may not affect characteristic lifetimes measurably.

Failed Samples

The trends for intermetallic precipitate coarsening and microstructural evolution of SAC alloys during accelerated thermal cycling have been discussed in numerous publications.[27,28,45–47] The backscattered electron image in Fig. 15 illustrates the accelerated intermetallic particle coarsening and recrystallization in the strain-localized region of the solder joint where crack propagation occurs. This image was taken from a metallographic cross section of a 192CABGA with SAC305 solder, tested at 0/100°C with a 10-min dwell time.[17] The combination of strain and temperature in this region promotes recrystallization and fatigue crack propagation. In the absence of higher strain, coarsening is much slower as evidenced by the smaller particles and higher particle density in the region adjacent to or below the crack. This pattern of microstructural evolution is characteristic of the thermal fatigue failure process in these Pb-free alloys and was described originally in detail by Dunford et al.[46]
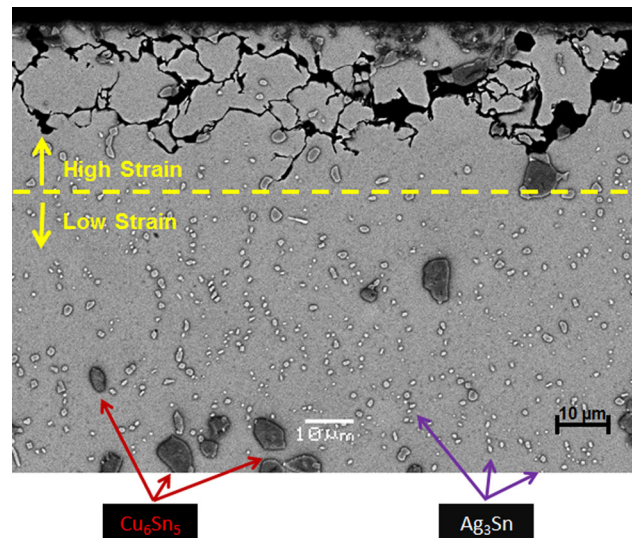

Fig. 15. An example of accelerated intermetallic particle coarsening in the strain-localized region of a 0/100°C SAC305, 192CABGA sample.

The metallographic failure analyses for the 192CABGA and 84CTBGA packages with high and low Ag alloys are shown in the optical photomicrographs in Figs. 16 and 17. Although the failure analysis results might have been compromised somewhat leaving the samples in the chamber until
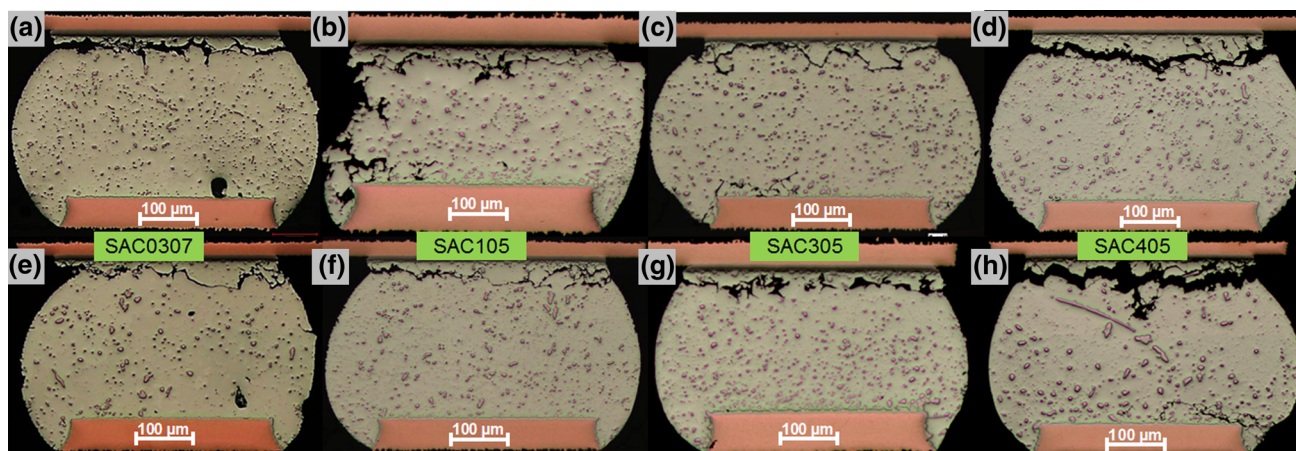
Fig. 16. Optical photomicrographs illustrating thermal fatigue damage in the 192CABGA package with alloys of various Ag contents and the 0/100°C ATC profile. (a–d) From a test using the 10-min dwell time. (e–h) From a test using the 60-min dwell. The fracture characteristics are typical of SAC alloy thermal fatigue for all combinations of dwell time and alloy.
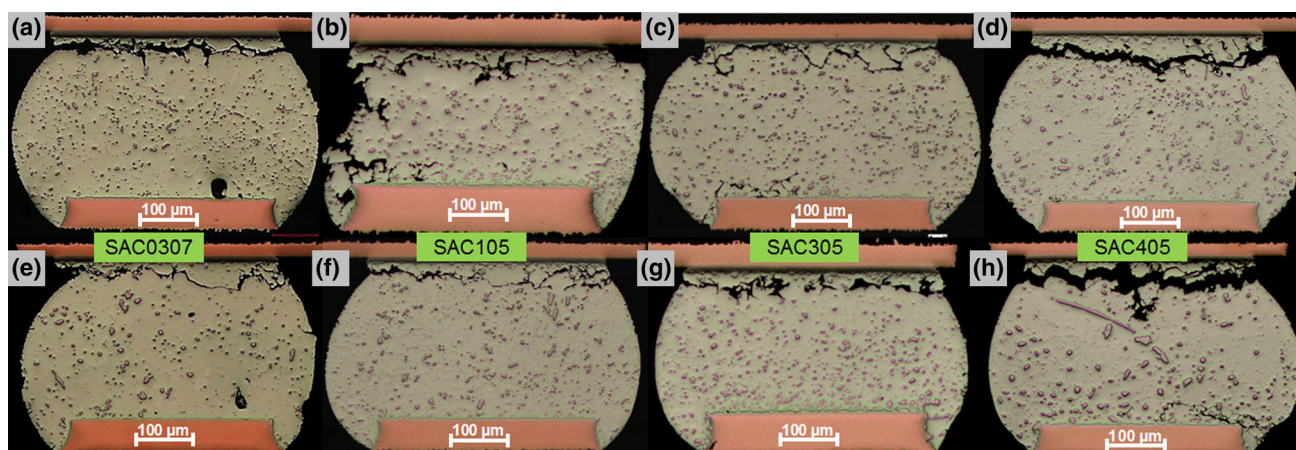

Fig. 17. Optical photomicrographs illustrating thermal fatigue damage in the 84CTABGA package with alloys of various Ag contents and the 0/100°C ATC profile. (a–d) From a test using the 10-min dwell time. (e–h) From a test using the 60-min dwell. The fracture characteristics and particle coarsening are similar for all alloys and both dwell times and are typical of thermal fatigue failure in SAC alloys.

all joints had failed, the crack nucleation and propagation mechanisms appear to be similar. The cracking is characterized by accelerated coarsening of the intermetallic compounds and recrystallization in high strain areas followed by sliding and rotation of the small grains resulting in crack initiation and propagation along the grain boundaries.[16–18,47] The fracture characteristics appear to be typical of SAC alloy thermal fatigue for all combinations of dwell time and alloy. The Ag$_3$Sn particle coarsening and Sn grain recrystallization in the strain-localized regions are shown in the SEM images in Fig. 18.

SUGGESTIONS FOR FUTURE STUDIES

This experimental program evaluated a wide range of Pb-free alloys using a number of standard and experimental accelerated thermal cycling profiles. Less emphasis was placed on understanding the relationship between microstructure and accelerated thermal cycling performance due to project resource limitations. As the project evolved, so did the industry awareness of microstructural evolution in Pb-free solders.

The following sections describe additional investigations and analyses that could be performed on accelerated thermal cycling test samples to provide a better understanding of the effect of microstructure on characteristic life in ATC testing. Important points are highlighted and some examples are provided. Analyses using extensive metallography and advanced microstructural techniques were beyond the scope of the project as originally defined. As the investigation progressed and additional information became available through the literature, the value of these techniques was recognized in order to understand the performance of alloys and correlate that performance with different test parameters such as package type, ATC profile, and dwell time. Therefore, it is recommended to include each of the
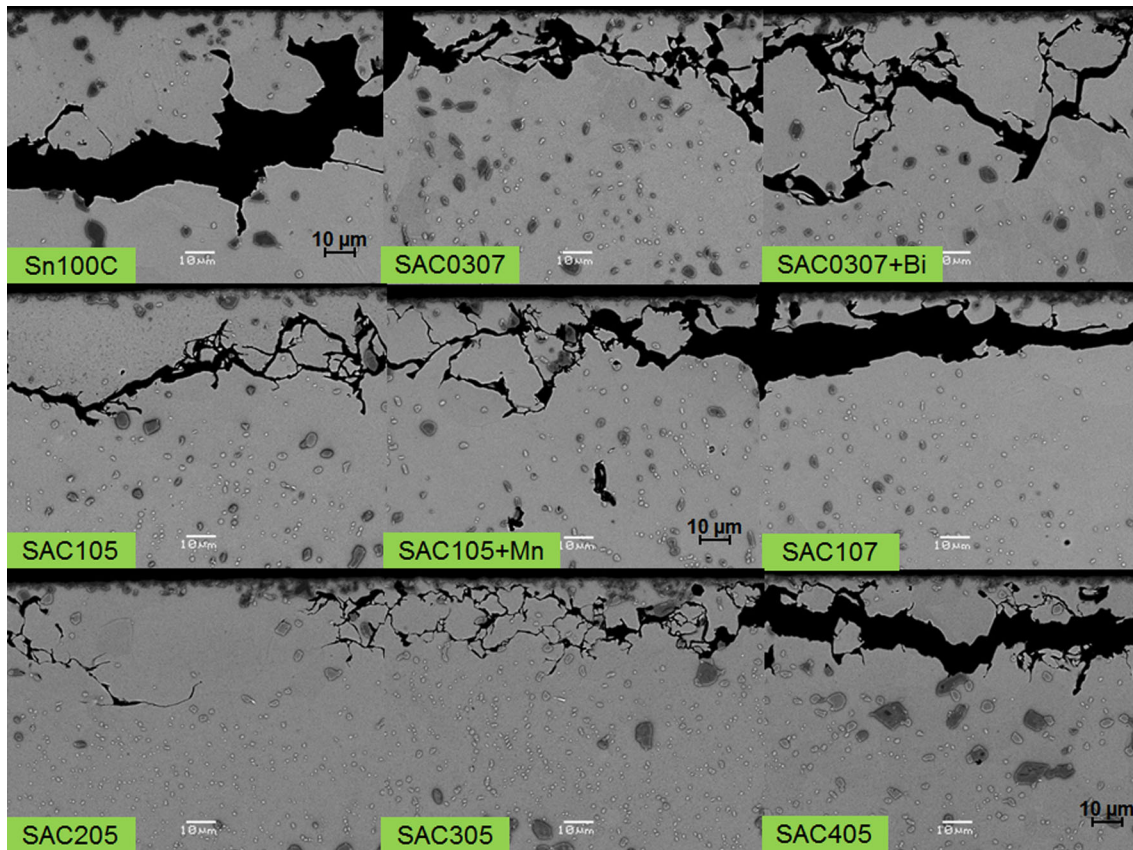
Fig. 18. SEM images showing Ag$_3$Sn particle coarsening and Sn grain recrystallization in multiple solder alloys resulting from damage accumulate during 0/100°C with 10-min dwell thermal cycling.

following aspects in future studies. It is also important to note that, in order to do a careful microstructural analysis, samples should be taken out of the accelerated thermal cycling chamber immediately after they fail. Leaving the samples in test for a long time after failure could considerably change the microstructure of the solder joint.

Measurement of Ag$_3$Sn Precipitates

It is well known that the morphology of Ag$_3$Sn precipitates, their number, and spacing, are important in determining the reliability of SnAgCu solder joints. Ag$_3$Sn precipitates which form in near-eutectic SnAgCu strengthen the Sn matrix material through a precipitate-hardening mechanism. A large number of closely spaced small particles are more effective obstacles to dislocation movement than the fewer larger and consequently more widely spaced particles that are left after coarsening processes. Several parameters such as solder composition, solidification temperature and cooling rate can affect the size and spacing of Ag$_3$Sn precipitate. In order to study the effect of precipitates on the fatigue lifetime, a quantitative analysis of the microstructure of the solder balls should be performed. Special care should be taken to distinguish between the Ag$_3$Sn, Cu$_6$Sn$_5$, Sn matrix and

polishing damage. An example of such work is shown in Fig. 19. Backscatter scanning electron images were taken from the center of an as-reflowed SAC 305, 192CTBGA component. The results in Table V show that the number, size and spacing of Ag$_3$Sn precipitate vary from the left to the right side of solder joint. This is expected as Sn nucleation in these samples occurs at only one point and, further from the nucleation point, the size of precipitates and dendrite arm spacing varies. It is possible to see changes in average precipitate sizes from sample to sample due to the different degree of undercooling for various joints. It is also known that the Ag$_3$Sn precipitates evolve at elevated temperatures and their size becomes larger while the smaller precipitates disappear (Ostwald Ripening). There are limited publications that show the quantification of precipitates in a careful manner and correlate them to the mechanical properties of solder joints.[48,49] However, no data exist to correlate such measurements to the ATC performance of solder joints.

Sn Grain Orientation and EBSD Analysis

In Pb-free SAC solder alloys, Sn is the major component of the alloys and β-Sn, which has a tetragonal unit cell, displays large anisotropies in its physical and mechanical properties, given the
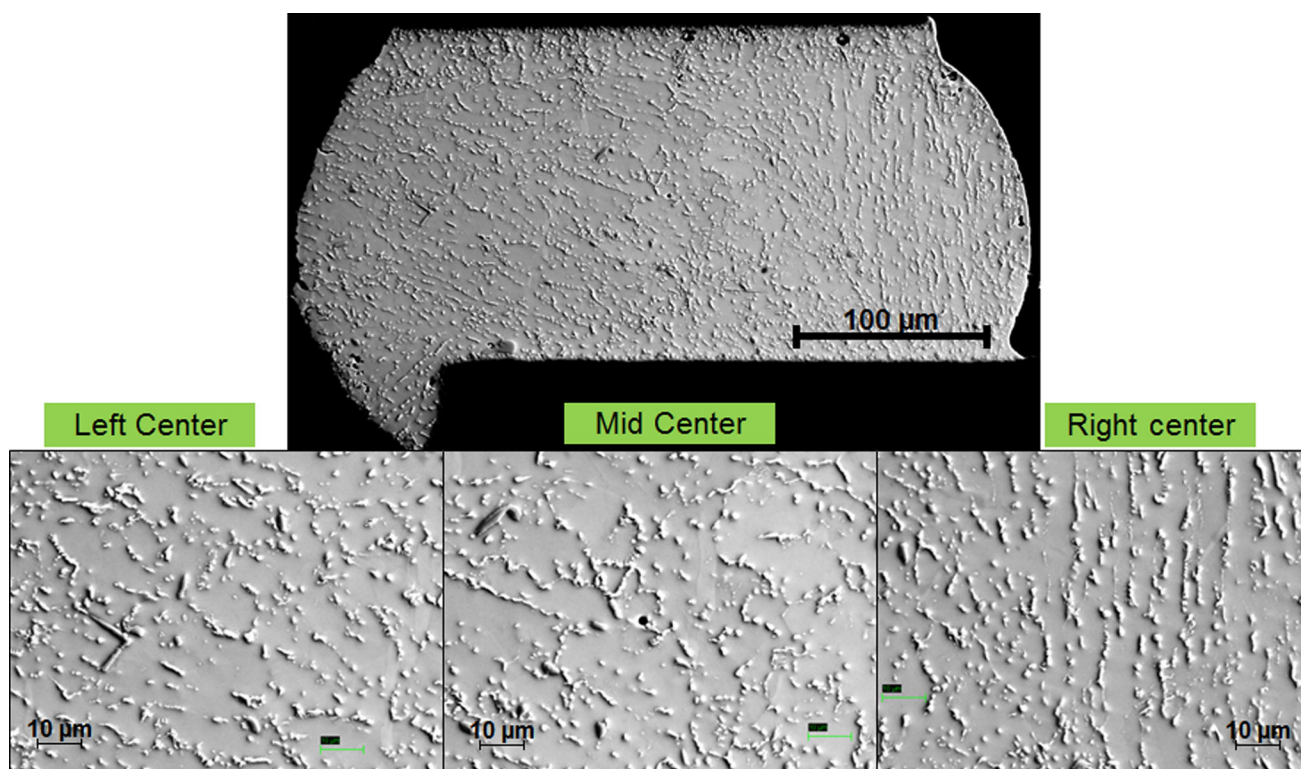
Fig. 19. Three high-resolution backscattered SEM images from the left-to-right side of a cross-section of an as-reflowed 84CTBGA joint that was assembled with Sn100C ball and SAC 305 paste. The size, number and spacing of Ag$_3$Sn precipitates were measured and are presented in Table V.

Table V. Number, size, area fraction and spacing of Ag$_3$Sn precipitates at left, center and right sides of as-reflowed solder joints to an 84CTBGA component

SN100C/SAC305	# of Ag$_3$Sn precipitates	Average size of precipitates (nm)	Area fraction of precipitates	Ag$_3$Sn precipitates spacing (nm)
Left center	682	591	5.3	2150
Mid center	634	577	4.8	2668
Right center	757	578	5.8	2322

The measurements were made on the images in Fig. 19.

marked anisotropies in the thermal expansion coefficient and Young's modulus of Sn, which vary by factors of two and three, respectively, with crystal direction.[50,51] Thus, the orientations of the Sn grains are a critical parameter in determining the thermomechanical response of SnAgCu solder joints.[24,44,47] Two common techniques to investigate the Sn grain morphology are polarized light microscopy and electron backscattered diffraction (EBSD). Sn exhibits birefringent properties, resulting in different colors for different crystal orientations under cross-polarized imaging. EBSD is a more powerful technique, and more time consuming, which can help determine the orientation of each Sn grain. Both techniques are useful to characterize the Sn grains after reflow and their

evolution during ATC test. Generally, during accelerated thermal cycling tests, strain-enhanced precipitate coarsening and recrystallization occur in high strain regions of the joint. A fatigue crack then starts to propagate along the network of grain boundaries through the recrystallized area until failure. The recrystallization of Sn during accelerated thermal cycling has been directly related to crack propagation in SAC solder joints.[35,46,47,52] Evidence of such behavior are portrayed in Figs. 20 and 21. The EBSD map (Fig. 21b) shows the orientations of grains clearly. Each color corresponds to one Sn grain orientation with the black regions indicating non-indexed areas, generally due to polishing damages or presence of Ag$_3$Sn and Cu$_6$Sn$_5$ precipitates. The EBSD map of failed samples
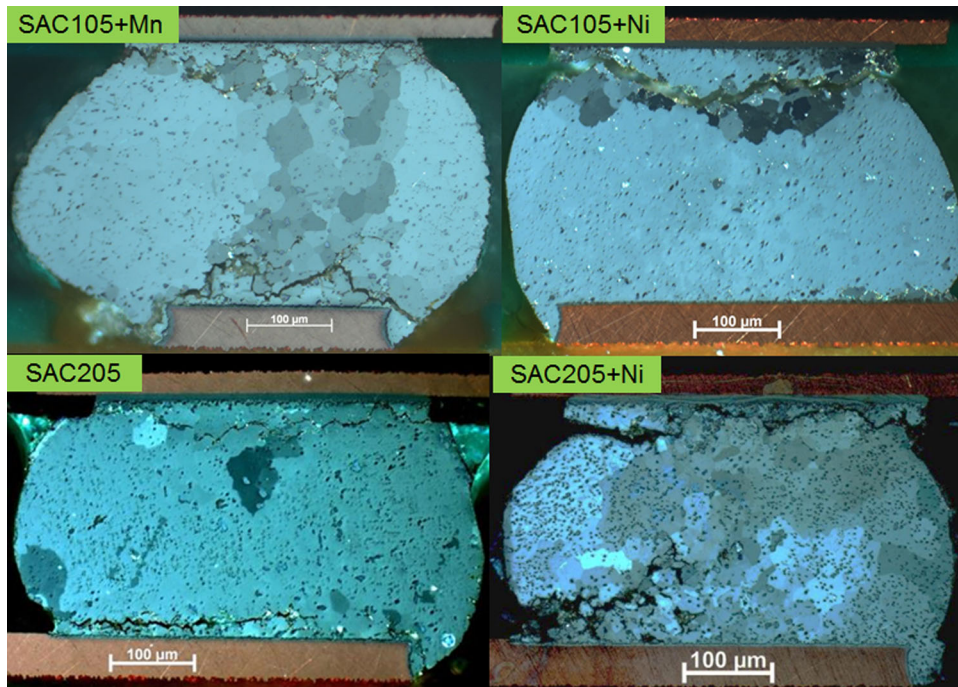
Fig. 20. Micrograph with crossed polarizers of failed joints to 192CABGA components. SAC105+Mn, SAC105+Ni, SAC 205, SAC205+Ni solder balls reflowed with SAC305 paste. The thermal cycle was 0/100°C with 10-min dwell.
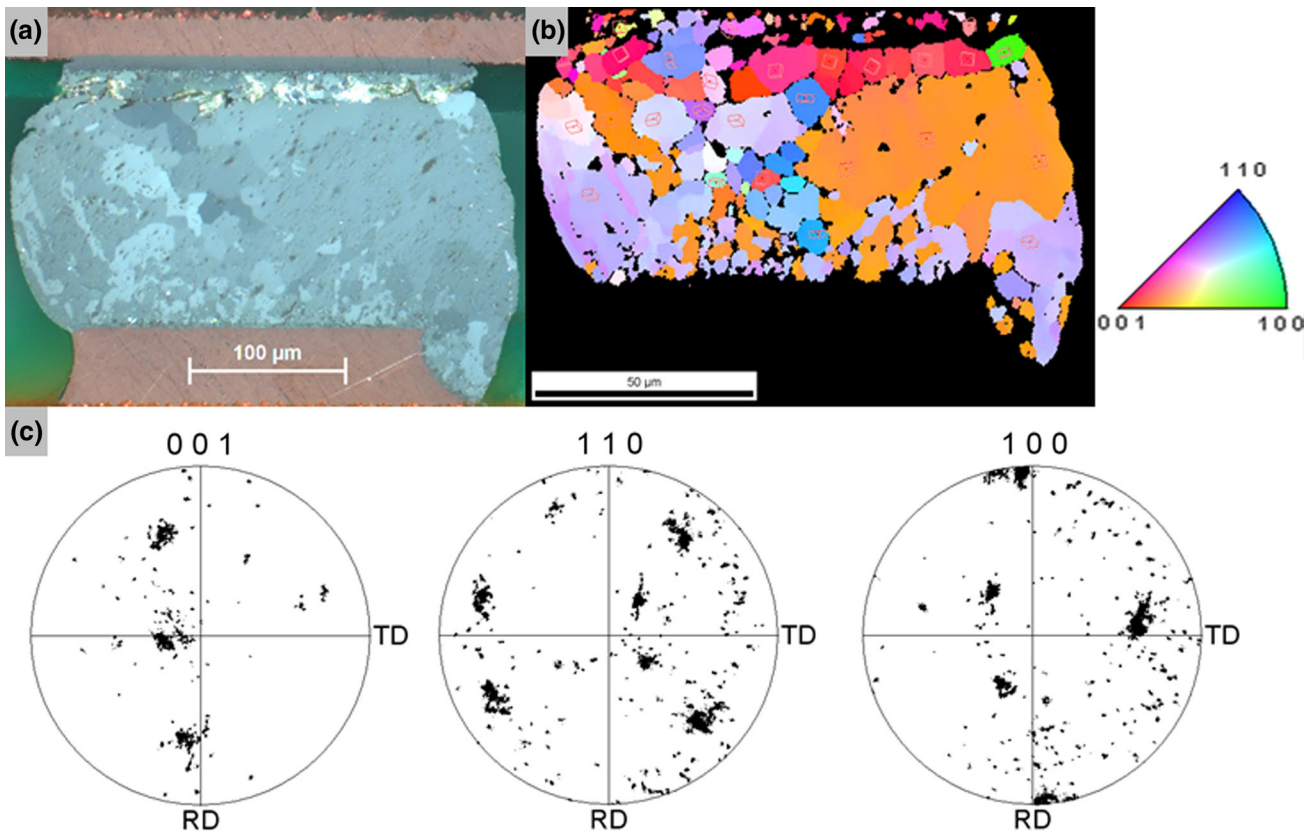

Fig. 21. Optical micrographs with (a) cross-polarizer, (b) EBSD of a failed SAC 305 joint to a 84CTBGA component showing the microstructural evolution in accelerated thermal cycling, and (c) pole figures showing the presence of three parent grains and newly formed recrystallized grains with different orientations.

shows the formation of new grains close to the component side where the strain is largest. Complete recrystallization across the joint is visible. Large Sn grains, such as those observed in the as-reflowed sample, are still visible. New grains with high-angle grain boundaries are formed as a result of accelerated thermal cycling. Such investigation on failed samples and also samples that are taken from the chamber at some percentage of their characteristic life could significantly help to understand the cause of early or late failure in solder joints, and also the potential effect of alloying elements on recrystallization and failure mechanism. In addition, it would be helpful to develop microstructurally adaptive models that can predict the lifetime of joints in ATC tests.

Undercooling Measurements and Quantifying the Sn Grain Morphology

It has been shown that the accelerated thermal cycling performance of SnAgCu solder joints are affected by differences in Sn grain morphology (i.e, beach-ball versus interlaced).[47] The results showed that relatively long lifetimes were observed for samples which initially displayed an interlaced Sn grain morphology, as opposed to the beach-ball Sn grain morphology. The Sn grain morphologies of several alloys in this study were quantified for both 192CABGA and 84CTBGA packages. All the joints at the outer row of as-reflowed samples were individually investigated to characterize their Sn grain morphology. Four different categories were defined to quantify the Sn grain morphologies (details have been provided in other publications[42,47]) The results are shown in Fig. 22. As expected, larger 192CABGA samples assembled with different alloys are more likely to show a beach-ball structure (single- or multi-grain) while smaller 84CTABGA samples show more partial interlaced and interlaced Sn grain morphologies. It seems the presence of some alloying elements such as Ni can promote the formation of an interlaced structure.[17]

Previous studies have shown that there is a correlation between solidification temperature and the Sn grain morphology in these near-eutectic SnAgCu samples. Generally, samples solidified at higher temperatures show beach-ball structure, while smaller samples that undercool more show interlaced Sn grain morphology.[34,44,53,54] The undercooling measurements of alloys investigated in this study are shown in Fig. 23. Generally, smaller samples (12 mil, 0.30 mm) showed a larger degree of undercooling compared to larger samples (18 mil, 0.46 mm). The effect of alloying element on undercooling data is not obvious from the current measurements. However, SN100C SAC107 and SACi alloys show considerably larger undercooling compared to all other alloysm and it is also worth noting that undercooling degrees could significantly change when spheres are attached to the component
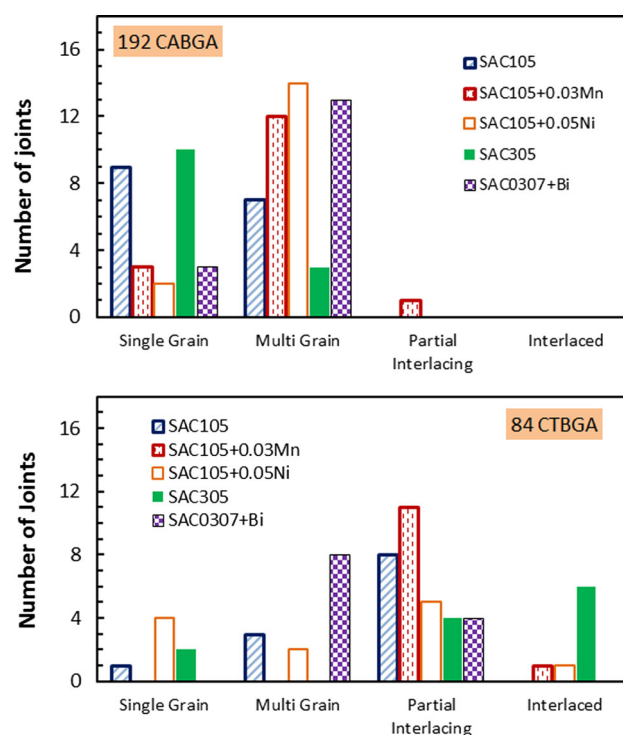

Fig. 22. The effect of joint volumes on the Sn grain structure of solder joints: (a) 192CABGA, and (b) 84CTBGA. For the larger joints to 192CABGA components there was a higher incidence of single- and multi-grain microstructures. Results are based on the examination of 16 joints to 192CABGA components and 12 to 84CTBGA components.

and PCB. The degree of undercooling will affect both the Sn grain morphology and also the size and distribution of precipitates. Thus, it is important to investigate the effect of alloying elements on solidification behavior of joints.

The above three points are just some examples to highlight the important aspects of SAC solder joints that need to be considered in order to correlate ATC performance to microstructure. Very careful planning to investigate each of the above-mentioned aspects is needed. Moreover, extensive metallography work is needed to obtain reasonably representative data for all various alloys and packages that will be studied.

Experimental Considerations

One of the most interesting findings to emerge from this study is that the strengthening effect of Ag content lessens dramatically as the severity of the accelerated thermal cycling increases, in terms of the difference between the temperature extremes (ΔT), the peak temperature of the thermal cycle, and the dwell time. The microstructural evolution of the Ag_3Sn particle coarsening that ultimately leads to failure is driven by a complex relationship between the strain generated during accelerated thermal cycling and the dwell time at the peak temperature. The effect of strain-enhanced coarsening is dramatic
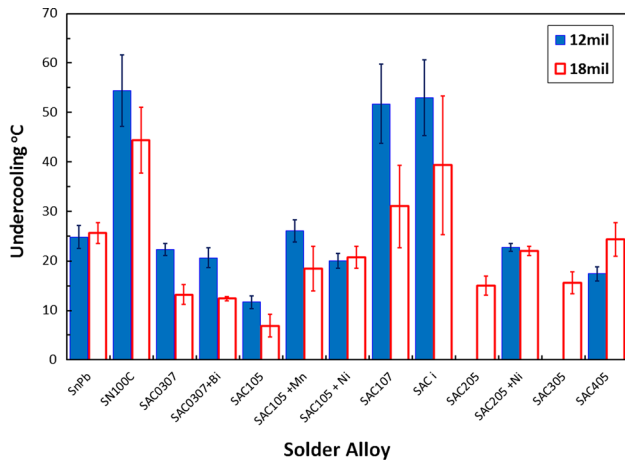
Fig. 23. Undercooling measurements of two different size free-standing solder alloys. The larger 18 mil (0.46 mm) sphere was used for the 192CABGA and the smaller 12 mil (0.30 mm) sphere was used for the 84CTBGA. The undercooling measurements are based on four DSC runs on three different samples, 12 measurements total, for each size and solder alloy.

(Fig. 15), but the relative effect of strain and temperature cannot be assessed independently. The Ag_3Sn particle coarsening also occurs throughout the cycle, not only during the peak temperature dwell. No doubt there is more to be learned about the acceleration of the damage mechanisms in these Sn-based, Pb-free solders. Additional accelerated thermal cycling tests of Sn-based Pb-free solders should include at least two different accelerated thermal cycling profiles, given the difference in performance measured with various thermal cycle profiles (Fig. 8). It may also be useful to include a so-called mildly accelerated thermal cycling profile in a test program. Mild profiles are characterized by reduced ΔT and temperature extremes matched closer to service conditions.

Because of the limited sample size for the test vehicles, almost all remained in the test chambers until the test was completed. Specific first failures could not be identified, and it is assumed that substantial further coarsening of Ag_3Sn occurred after failure. Previous work has demonstrated that investigations of microstructural evolution preceding crack initiation, recrystallization, and failure can benefit from inclusion of additional components in the test plan to enable samples to be taken from the chamber at some percentage of their characteristic life for analysis.[42,47] This could help to understand the cause of early or late failure in solder joints and also the potential effect of alloying elements on recrystallization and the failure mechanism.

The two components used in this experiment are good candidates for additional alloy evaluations because of the large amount of available data for these components. However, the high internal strain of these two packages may have overshadowed some

thermal behavior, and additional test plans should consider the addition of a larger body, lower strain, plastic ball grid array test vehicle.

For additional alloy tests, it is recommended that board level attachment be performed using solder paste that matches the composition of the solder ball. Alternately, board level attachment could be done with tacky flux. Using either type of surface mount process will avoid altering the base alloy composition (Table III).

DEVELOPMENT OF NEW ALLOYS FOR HIGH RELIABILITY APPLICATIONS

Currently, two prominent paths are being pursued with third-generation solder alloy development regarding electronic applications. In one case, alloys with Ag content lower than SAC305 are being developed to address needs for better drop/shock resistance, lower processing (melting) temperature, and lower cost. These alloys are relevant for consumer applications and complex telecommunication applications requiring lower temperature assembly. In the other case, second-generation, high Ag content alloys are being modified with various alloying additions to improve thermal fatigue performance under conditions of severe accelerated thermal cycling and increase resistance to damage from high strain rate mechanical loading. These alloys are relevant for military, aerospace, and automotive applications.

These third-generation Pb-free alloys are characterized by significant additions of alloying elements such as Bi, Sb, and In. Most of these alloys are far from eutectic solidification and are characterized by melting ranges as much as 10–15°C. Alloys with these large so-called pasty ranges were previously considered unsuitable as solders, but are now given consideration due to their other desirable properties. While the current results confirmed that Ag can dramatically increase characteristic life in relatively mild accelerated thermal cycling, 0/100°C, it also found that it is much less effective in more severe conditions (Fig. 8). Even in relatively mild accelerated thermal cycling conditions, the characteristic life drops dramatically when the dwell time increases from 10 min to 60 min, the dwell time which is probably more representative of actual service conditions (Fig. 7).

These new alloys are targeted for use in harsh environments requiring resistance to both thermal-mechanical (accelerated thermal cycling) and mechanical (vibration, bending, and shock) loading. The alloys are being designed to improve toughness of interfacial intermetallic layers and provide solid solution strengthening to compensate for the loss of strength once the Ag_3Sn particles coarsen. In applications such as the engine compartment of motor vehicles where extreme thermal cycles and long dwell are common, it has been necessary to look for strengthening mechanisms that better

survive extremes of temperature, strain and dwell. While solid solution-strengthening by additions of Bi is also effective, it is not sufficient, and the other strengthening option, the introduction of additional precipitates, is being employed. Sb, which forms an additional intermetallic phase as well as providing further solid solution strengthening of the Sn, is being incorporated along with the Bi. The Ni level can also be increased to the point where an additional Ni intermetallic phase contributes to strengthening. The first commercial alloy of this type to emerge was the Innolot alloy, which is SAC387 modified with 3% Bi, 1.4% Sb, and 0.05% Ni.[55] Reliability testing and evaluation of third-generation Pb-free alloys is expected to be even more difficult than testing of the second-generation SAC alloys which dominate the existing consortia programs. It will be necessary to evaluate resistance to drop and shock loading, and accelerated thermal cycling must be evaluated over a wider range of cycling conditions. Further challenges are expected with basic microstructural characterization and failure analysis due to the compositional complexity of the new alloys.

CONCLUSION

The findings from the Alloy Characterization Project and Universal AREA Consortia research programs provide valuable guidance for applications in the electronics industry and for understanding the accelerated thermal cycling performance of Pb-free solders. Alloys based on the SnAgCu eutectic system have made it possible for most consumer electronics, and much of the electronics for which the EU RoHS Directive had granted exemption, to transition to Pb-free solder assembly without encountering significant reliability issues. Certainly, the results obtained indicate that all the Pb-free solders are more reliable in accelerated thermal cycling than the SnPb alloy they have replaced. The experiments confirmed the direct relationship between Ag content and the characteristic lifetime (reliability) in accelerated thermal cycling of BGA solder joints. No consistent effect of microalloying additions of Ni, Mn and Bi was reported. The lack of any significant effect of the Ni is not unexpected given that, in the soldered joint, this element is concentrated in the Cu_6Sn_5 phase, most of which is located at the interface between the solder and the copper substrate. The effects of Mn are not clearly known; however, no significant improvements in ATC test of Mn doped alloy were observed. Bi would have some solid solution strengthening effect but, in the commercial alloy included in this test program, the level was so low that its effect would be too small to be detected.

A significant finding is that the beneficial effect of Ag on accelerated thermal cycling reliability (measured by characteristic lifetime) diminishes as the severity of the accelerated thermal cycling, defined by greater ΔT, higher peak temperature, and longer dwell time, increases. The implication of this observation is that, while Ag is very effective in increasing reliability in relatively mild accelerated thermal cycling conditions, e.g. 0/100°C with 10-min dwells with components that do not generate excessive strain differentials, for more severe conditions reliability could be increased if there were an alternative or additional strengthening mechanism that is not vulnerable to the degradation mechanisms which reduce the effectiveness of Ag as a solder alloy strengthening mechanism. This problem is being addressed through the development of third-generation Pb-free alloys which are characterized by significant additions of alloying elements such as Bi, Sb, and In. New test programs are needed to evaluate the accelerated thermal cycling performance of these complex third-generation Pb-free alloys. These alloys present more challenges for microstructural analysis due to their compositional complexity. It would be prudent to support any new test program with the resources to perform quantitative metallography on precipitates, EBSD for measurement of Sn grain orientation and morphology and understanding the recrystallization behavior, and also DSC to characterize the melting and undercooling behavior of the alloys.

ACKNOWLEDGEMENTS

REFERENCES

1. W. Engelmaier, *Soldering Surf. Mount Technol.* 1, 14 (1989).
2. Round Robin Testing and Analysis of Lead Free Solder Pastes with Alloys of Tin, Silver and Copper: Final Report,

IPC Solder Products Value Council, Lead Free Technical Subcommittee (2005).

3. S. Terashima, Y. Kariya, T. Hosoi, and M. Tanaka, *J. Electron. Mater.* 32, 1527 (2003).

4. S.K. Kang, Paul Lauro, Da-Yuan Shih, D.W. Henderson, T. Gosselin, J. Bartelo, S.R. Cain, C. Goldsmith, K.J. Puttlitz, and T.K. Hwang, *Proceedings of the Electronic Components and Technology Conference* (Las Vegas, NV, 2004), pp. 661–667.

5. R. Coyle, M. Reid, C. Ryan, R. Popowich, P. Read, D. Fleming, M. Collins, J. Punch, and I. Chatterji, *Proceedings of the Electronic Components and Technology Conference* (IEEE, Piscataway, NJ, 2009), pp. 423–430.

6. G. Henshall. J. Bath, S. Sethuraman, D. Geiger, A. Syed, M.J. Lee, K. Newman, L. Hu, D.H. Kim, W. Xie, W. Eagar, and J. Waldvogel, *Proceedings of the Institute of Printed Circuits* (2009), pp. S05–S03.

7. K. Nogita, J. Read, T. Nishimura, K. Sweatman, S. Suenaga, and A.K. Dahle, *Mater. Trans.* 46, 2419 (2005).

8. I.E. Anderson, *J. Mater. Sci.: Mater. Electron.* 18, 55 (2007).

9. S.K. Kang, *IBM Research Report, RC25045* (NY: Yorktown Heights, 2010).

10. IPC-9701A, *Institute of Printed Circuits* (Bannockburn, IL, 2006).

11. G. Henshall, J. Miremadi, R. Parker, R. Coyle, J. Smetana, J. Nguyen, W.G Liu, K. Sweatman, K. Howell, R.S. Pandher, D. Daily, M. Currie, T. Lee, J. Silk, B. Jones, S. Tisdale, F. Hua, M. Osterman, B. Barthel, T. Sack, P. Snugovsky, A. Syed, A. Allen, J. Arnold, D. Moore, G. Chang, and E. Benedetto, *Proceedings of the SMTA International Conference* (Orlando, FL, 2012), pp. 335–347.

12. R. Parker, R. Coyle, G. Henshall, J. Smetana, and E. Benedetto, *Proceedings of the SMTA International Conference* (Orlando, FL, 2012), pp. 348–358.

13. K. Sweatman, K. Howell, R. Coyle, R. Parker, G. Henshall, J. Smetana, E. Benedetto, W. Liu, R.S. Pandher, D. Daily, M. Currie, J. Nguyen, T. Lee, M. Osterman, J. Miremadi, A. Allen, J. Arnold, D. Moore, and G. Chang, *Proceedings of the SMTA International Conference* (Orlando, FL, 2012), pp. 359–375.

14. R. Coyle, R. Parker, G. Henshall, M. Osterman, J. Smetana, E. Benedetto, D. Moore, Graver Chang, J. Arnold, and T. Lee, *Proceedings of the SMTA International Conference* (Orlando, FL, 20120, pp. 376–389.

15. R. Coyle, R. Parker, M. Osterman, S. Longgood, K. Sweatman, E. Benedetto, A. Allen, E. George, J. Smetana, K. Howell, and J. Arnold, *Proceedings of the SMTA International Conference* (Ft. Worth, TX, 2013), pp. 470–489.

16. R. Coyle, R. Parker, B. Arfaei, K. Sweatman, K. Howell, S.T. Longgood, and E. Benedetto, *Proceedings of the SMTA International Conference* (Ft. Worth, TX, 2013), pp. 490–414.

17. R. Coyle, R. Parker, B. Arfaei, F. Mutuku, K. Sweatman, K. Howell, S. Longgood, and E. Benedetto, *Proceedings of the Electronic Components and Technology Conference* (IEEE, Orlando, FL, 2014), pp. 425–440.

18. K. Sweatman, R. Coyle, R. Parker, K. Howell, E. Benedetto, J. Smetana, A. Allen, W. Lui, and J. Silk, *Proceedings of the SMTA International Conference* (Chicago, IL, 2014), pp. 561–574.

19. R. Coyle, R. Parker, E. Benedetto, K. Howell, K. Sweatman, S. Longgood, J. Smetana, A. Allen, P. Read, B. Arfaei, and F. Mutuku, *Proceedings of the SMTA International Conference* (Chicago, IL, 2014), pp. 547–560.

20. E. Bradley, C.A. Handwerker, J. Bath, R.D. Parker, and R.W. Gedney, *Lead-free electronics* (Chichester: Wiley, 2007).

21. E. George, M. Osterman, M. Pecht, and R. Coyle, *Proceedings of the International Symposium on Microelectronics* (San Diego, CA, 2012).

22. S. Yoon, Z. Chen, M. Osterman, B. Han, and A. Dasgupta, *Proceedings of the Electronics Components and Technology Conference* (Lake Buena Vista, FL, 2005), pp. 1210–1214.

23. Y. Zhang, Z. Cai, J.C. Suhling, P. Lal, and M. Bozak, *Proceedings of the Electronic Components and Technology Conference* (Lake Buena Vista, FL, 2008), pp. 99–112.

24. T. Bieler, H. Jiang, L. Lehman, T. Kirkpatrick, E. Cotts, and B. Nandagopal, *I.E.E.E. Trans. Compon. Packag. Technol.* 31, 370 (2008).

25. R. Darveaux, C. Reichman, C. Berry, W.-S. Hsu, and A. Syed, *Proceedings of the Electronic Components and Technology Conference* (Lake Buena Vista, FL, 2008), pp. 113–122.

26. S.K. Kang, P. Lauro, D. Shih, D.W. Henderson, T. Gosselin, J. Bartelo, S.R. Cain, C. Goldsmith, K.J. Puttlitz, and T. Hwang, *Proceedings of the Electronic Components and Technology Conference* (Las Vegas, NV, 2004), pp. 661–667.

27. R. Coyle, J. Osenbach, M. Collins, H. McCormick, P. Read, D. Fleming, R. Popowich, J. Punch, M. Reid, and S. Kummerl, *I.E.E.E. Trans. Compon. Packag. Technol.* 1, 1583 (2011).

28. R. Coyle, P. Read, H. McCormick, R. Popowich, and D. Fleming, *J. SMTA* 25, 28 (2011).

29. R. Coyle, H. McCormick, J. Osenbach, P. Read, R. Popowich, D. Fleming, and J. Manock, *J. SMTA* 24, 27 (2011).

30. R. Coyle, R.t Kinyanjui, P. Read, J. Shirey, D. Fleming, M. Abtew, R. Popowich, I. Muntele, and J. Manock, *Proceedings of the SMTA International Conference* (Orlando, FL, 2010), pp. 548–558.

31. T. Lee and H. Ma, *Proceedings of the Electronic Components and Technology Conference* (San Diego, CA, 2012), pp. 477–482.

32. J.-P. Clech, G. Henshall, and J. Miramadi, *Proceedings of the SMTA International Conference* (San Diego, CA, 2009), pp. 393–408.

33. J. Wilcox, R. Coyle, L. Lehman, and J. Smetana, *Proceedings of the SMTA International Conference* (Chicago, IL, 2014), pp. 122–133.

34. R. Kinyanjui, L.P. Lehman, L. Zavalij, and E. Cotts, *J. Mater. Res.* 20, 2914 (2005).

35. L. Yin, L. Wentlent, L. Yang, B. Arfaei, A. Qasaimeh, and P. Borgesenn, *J. Electron. Mater.* 41, 241 (2011).

36. F. Lin, W. Bi, G. Ju, W. Wang, and X. Wei, *J. Alloys Compd.* 509, 6666 (2011).

37. G. Henshall, R. Healy, R.S. Pander, K. Sweatman, K. Howell, R. Coyle, T. Sack, P. Snugovsky, S. Tisdale, and F. Hua, *J. SMTA* 21, 11 (2008).

38. R. Coyle, J. Osenbach, P. Read, H. McCormick, D. Fleming, R. Popowich, M.L Reid, J. Punch, M. Collins, R. Kinyanjui, and S. Kummerl, *Proceedings of the SMTA International Conference* (San Diego, CA, 2009), pp. 384–392.

39. K.-W. Moon, W.J. Boettinger, U.R. Kattner, F.S. Biancaniello, and C.A. Handwerker, *J. Electron. Mater.* 29, 1122 (2000).

40. K. Nogita and T. Nishimura, *Scr. Mater.* 59, 191 (2008).

41. B. Arfaei, L. Wentlent, S. Joshi, A. Alazzam, T. Tashtoush, M. Halaweh, S. Chivukula, L. Yin, M. Meilunas, E. Cotts, and P. Borgesen, *Proceedings of the IEEE Intersociety Conference on Thermal and Thermomechanical Phenomena in Electronic Systems* (2012), pp. 392–398.

42. B. Arfaei, L. Wentlent, S. Joshi, M. Anselm, and P. Borgesen, *Proceedings of the ASME International Mechanical Engineering* (2012).

43. T. Bieler, H. Jiang, L. Lehman, T. Kirkpatrick, and E. Cotts, *Proceedings of the Electronic Components and Technology Conference* (San Diego, CA, 2006), pp. 1462–1467.

44. B. Arfaei, N. Kim, and E.J. Cotts, *J. Electron. Mater.* 41, 362 (2012).

45. J. Manock, R. Coyle, B. Vaccaro, H. McCormick, R. Popowich, D.P. Read, J. Osenbach, and D. Gerlach, *J. SMTA* 21, 36 (2008).

46. S. Dunford, S. Canumalla, and P. Viswanadham, *Proceedings of the Electronic Components and Technology Conference* (Las Vegas, NV, 2004), pp. 726–736.

47. B. Arfaei, S. Mahin-Shirazi, S. Joshi, M. Anselm, P. Borgesen, E. Cotts, J. Wilcox, and R. Coyle, *Proceedings of the Electronic Components Technology Conference* (Las Vegas, NV, 2013).

48. M. Maleki, J. Cugnoni, and J. Botsis, *J. Electron. Mater.* 43, 1026 (2014).

49. B. Arfaei and E. Cotts, *J. Electron. Mater.* 38, 2617 (2009).
50. P.W. Bridgman, *Proc. Am. Acad. Arts Sci.* 60, 305 (1925).
51. J.A. Rayne and B.S. Chandrasekhar, *Phys. Rev.* 120, 1658 (1960).
52. T.T. Mattila and J.K. Kivilahti, *I.E.E.E. Trans. Compon. Packag. Technol.* 33, 629 (2010).
53. B. Arfaei, M. Benedict, and E. Cotts, *J. Appl. Phys.* 114, 173506 (2013).
54. L.P. Lehman, Y. Xing, T.R. Bieler, and E. Cotts, *Acta Mater.* 58, 3546 (2010).
55. H.J. Albrecht, P. Frühauf, and K. Wilke, *Proceedings of the SMTA International Conference* (San Diego, CA, 2009), pp. 308–316.